

# Collapse and fragmentation of molecular clouds under pressure

Kastytis Zubovas, Kostas Sabulis and Rokas Naujalis

*Center for Physical Sciences and Technology, Savanorių 231, Vilnius LT-02300, Lithuania*

*E-mail:* kastytis.zubovas@ftmc.lt

31 May 2021

## ABSTRACT

Recent analytical and numerical models show that AGN outflows and jets create ISM pressure in the host galaxy that is several orders of magnitude larger than in quiescent systems. This pressure increase can confine and compress molecular gas, thus accelerating star formation. In this paper, we model the effects of increased ambient ISM pressure on spherically symmetric turbulent molecular clouds. We find that large external pressure confines the cloud and drives a shockwave into it, which, together with instabilities behind the shock front, significantly accelerates the fragmentation rate. The compressed clouds therefore convert a larger fraction of their mass into stars over the cloud lifetime, and produce clusters that are initially more compact. Neither cloud rotation nor shear against the ISM affect this result significantly, unless the shear velocity is higher than the sound speed in the confining ISM. We conclude that external pressure is an important element in the star formation process, provided that it dominates over the internal pressure of the cloud.

**Key words:** stars:formation — star clusters:formation — molecular clouds

## 1 INTRODUCTION

Under normal circumstances, star formation is a slow process: on all spatial scales larger than single pre-stellar cores, almost independently of environment, only 1 – 3% of the molecular gas available for star formation is converted into stars every dynamical time (McKee & Ostriker 2007; Krumholz & Tan 2007; Krumholz et al. 2012). Molecular clouds have lifetimes that depend on their sizes, with the smallest clouds ( $R_{\text{cl}} \sim 1 - 3$  pc) dispersing after only 1 – 3 Myr due to stellar feedback (Allen et al. 2007; Hartmann et al. 2001), while the largest clouds survive up to  $\sim 30$  Myr (Williams & McKee 1997; Kawamura et al. 2009; Dobbs & Pringle 2013). Despite these differences in absolute values, the cloud lifetimes are typically equal to a few crossing times, defined as the cloud size divided by the velocity dispersion in the cloud (Dobbs & Pringle 2013), and similar to the dynamical times for turbulence-supported clouds. As a result, most clouds only convert  $< 10\%$  of their gas mass into stars before dispersing (Williams & McKee 1997; Hartmann et al. 2001; Kawamura et al. 2009; Dobbs & Pringle 2013).

Star formation must be more efficient than this in order to produce clusters that remain bound after the parent cloud is dispersed; some simulations show that  $\sim 10 - 30\%$  of the cloud mass must be converted into stars (e.g.

Geyer & Burkert 2001; Baumgardt & Kroupa 2007). On the other hand, the hierarchical structure of the ISM implies that stars forming in the densest parts of the molecular clouds are more bound than the cloud as a whole, and so can form bound star clusters even though the global star formation efficiency stays low (Kruijssen 2012, 2013). On a global scale, it has been suggested that gravitational binding of massive clouds ( $M \gtrsim 7 \times 10^6 M_{\odot}$ ) might be enough to withstand stellar feedback until enough gas is converted into stars (Kroupa & Boily 2002; Bressert et al. 2012), leading to formation of globular clusters, while less massive clouds probably have to be compacted in some way in order to form stars more rapidly (Escala & Larson 2008; Larsen 2010). However, these suggestions are unlikely to be correct, since they predict a cutoff of cluster populations at low masses, which is not observed (Fall & Chandar 2012; Bastian et al. 2012a,b). Overall, a picture emerges wherein regions of high density are important for the formation of bound star clusters, but those regions do not necessarily encompass whole clouds.

Several authors have suggested that the star formation rate is ultimately governed by self-regulation, for example a balance between pressure created by stellar feedback and self-gravity of the gas (e.g., Thompson et al. 2005). If that is the case, then an increase in the pressure of the ISM surrounding the cloud should result in an in-

crease of the star formation rate, as suggested recently by, e.g., Zubovas et al. (2013). Numerous recent models of the effect of AGN jets (Silk 2005; Gaibler et al. 2012) and outflows (Ciotti & Ostriker 2007; Nayakshin & Zubovas 2012; Zubovas et al. 2013; Ishibashi & Fabian 2012) upon the host galaxy ISM suggest that these processes can compress molecular gas to pressures several orders of magnitude higher than typically found in the hot phase ISM of quiescent galaxies. If this pressure translates into a linear increase in star formation rate, gas-rich AGN hosts may experience starbursts with star formation rates of several hundred  $M_{\odot} \text{ yr}^{-1}$  (e.g. Drouart et al. 2014).

Although the connection between higher ambient pressure and an increased star formation rate seems robust, it rests on several assumptions. First of all, it assumes that external pressure creates more favourable conditions for star formation, i.e. that star formation can be triggered by a pressure increase. The second assumption is that there is enough material that can readily react to an increase in pressure by forming stars, so that external pressure accelerates ongoing star formation. Finally, the connection requires a steady state to be established: star formation must not increase to such rates that molecular gas is exhausted before feedback can establish self-regulation. These assumptions cannot be tested in large-scale models, because they require analysis of gas dynamics and fragmentation on scales of molecular clouds, below the typical resolution of galaxy-wide numerical simulations.

In this paper, we present results of numerical SPH simulations of spherically symmetric turbulent clouds embedded in a hot ISM. We track the collapse and fragmentation of the clouds, showing that under pressure, fragmentation is caused by a combined action of a shockwave driven into the cloud and instabilities behind it, leading to much higher fragmentation rates than in uncompressed cloud. The net effect of external compression is that confined clouds collapse and fragment on a timescale shorter than the analytically-derived cloud-crushing timescale  $t_{\text{cr}} \simeq t_{\text{dyn}} (1 + P_{\text{ISM}}/P_{\text{grav}})^{-1/2}$ , where  $P_{\text{grav}}$  is the dynamical pressure of the cloud material necessary to overcome gravitational collapse, while  $P_{\text{ISM}}$  is the external pressure. Strongly compressed clouds fragment and turn a significant fraction of their mass into sink particles in  $t < 1 \text{ Myr}$ , before the cloud can begin to disperse due to stellar feedback. Furthermore, external pressure may confine even gravitationally unbound clouds, suggesting that compressed clouds may survive for longer even in the presence of stellar feedback or following the passage of an AGN shockwave. The resulting cluster of sink particles forming in our compressed cloud simulations is more massive and compact than the cluster born in uncompressed models. We conclude that external pressure enhances star formation in the cold ISM and produces clusters that are likely to survive for longer periods of time.

The paper is organised as follows. We begin by describing in more detail the physical basis of the connection between AGN activity and enhanced star formation (Section 2). Next, in Section 3, we present analytical estimates of the effect of external pressure on the cloud. In Section 4, we describe the set up of numerical simulations, while their results are shown in Section 5. Discussion of our findings

and their implications is presented in Section 6. Finally, we summarize and conclude in Section 7.

## 2 POSITIVE AGN FEEDBACK ON STAR FORMATION

The general picture of AGN effect upon the host galaxy is that of negative feedback. AGN jets or wide-angle outflows heat the gas and push it out of the host galaxy, quenching the star formation process (McNamara & Nulsen 2007; Feruglio et al. 2010; Fabian 2012). There is growing evidence, however, that the real picture is more complex, and that star formation can be enhanced by AGN activity as well.

One process through which AGN activity can enhance star formation is the increase in hot phase ISM pressure. Simple photoionization and Compton heating by the AGN radiation field can increase the temperature of the diffuse gas to  $10^7 \text{ K}$  or more. Using a typical ISM density of  $n_{\text{ISM}} = 1n_0 \text{ cm}^{-3}$ , we find that the distance to which the gas is heated efficiently is (Sazonov et al. 2004)

$$R_{\text{heat}} \simeq \left( \frac{200L_{\text{AGN}}}{n_{\text{ISM}}T_{\text{ISM}}} \right)^{1/2} \simeq 140L_{46}^{1/2}n_0^{-1/2}T_7^{-1/2} \text{ pc}, \quad (1)$$

where  $L_{46} \equiv L_{\text{AGN}}/10^{46} \text{ erg s}^{-1}$  is the AGN luminosity and  $T_7 \equiv T/10^7 \text{ K}$  the ISM temperature. The only clouds affected by direct AGN heating are those close to the centre of the galaxy. Furthermore, these clouds are themselves exposed to the dissociating and ionising AGN radiation. They can be heated, maintaining pressure equilibrium with the surroundings and losing molecular gas, leading to a lower star formation rate. Observations do not show either enhancement or suppression of star formation in clouds located in the centres of AGN hosts (Davies et al. 2005), so we believe that any effect due to direct heating is small.

A more promising approach for increasing the ISM pressure is shock heating. Shocks can be caused by a variety of processes, such as tidal interactions with companion galaxies (Ricker 1998) and ram pressure stripping in galaxy clusters (Bekki et al. 2002; Bekki & Couch 2003). AGN can also create shocks in the ISM by heating it rapidly via jets (Gaibler et al. 2012) and/or outflows (Zubovas & King 2012). The physical model we use in this paper is based on predictions of these positive AGN feedback models, and considers three situations how AGN jets and/or outflows can interact with cold dense gas.

A high-pressure outflow (created by either wind or jet) can overtake dense clumps of gas and compress them. The outflow expands with a velocity of order  $10^3 \text{ km/s}$  (Zubovas & King 2012), corresponding to a shock temperature of order  $10^7 - 10^8 \text{ K}$ . This causes the pressure inside an energy-driven AGN outflow to be 2-3 orders of magnitude higher than typical hot ISM pressure (Nayakshin & Zubovas 2012; Zubovas et al. 2013). Observed jet-inflated cocoons in radio galaxies have similarly high pressures (Begelman & Cioffi 1989; Gaibler et al. 2012). The interaction between a dense cloud and the outflow is very similar to the interaction of a cloud with a passing shockwave (e.g., Klein et al. 1994), except that the material behind the shockwave compresses the cloud further.

An expanding outflow is generally thermally unstable, can cool and form clouds (Nayakshin & Zubovas 2012; Zubovas & King 2014). These clouds form in pressure equilibrium with the surrounding flow and hence are not necessarily bound by their own gravity. A similar scenario was considered by Elmegreen & Efremov (1997), who found an increase in the star formation efficiency of clouds forming in high-pressure environments.

Finally, the outflow expanding in the diffuse gas of the galactic bulge and halo compresses the galactic disc. This creates a secondary shockwave passing into the disc and compressing the clouds there (Zubovas et al. 2013). The shockwave can develop a complex morphology due to the uneven density distribution of the disc ISM and therefore the clouds experience a wide range of shockwave velocities passing through them.

In the next section, we make analytic estimates of the effect of external pressure in these three situations, starting with the simplest, if somewhat unrealistic, scenario of negligible lateral velocity of the shockwave.

### 3 PRESSURE-ENHANCED CLOUD COLLAPSE

#### 3.1 Cloud confinement by external pressure

Here we make rough estimates regarding the effect that external pressure has on the internal dynamics of a molecular cloud in the various configurations discussed above. We scale all results to a cloud of mass  $M = 10^5 M_\odot$ ; this is a typical, if somewhat massive, example of a molecular cloud in the Milky Way (Roman-Duval et al. 2010). Using the Larson (1981) and Solomon et al. (1987) relations, we find the linear size of the cloud to be  $L \sim 17$  pc, so we choose the cloud radius as  $R = 10$  pc  $\sim L/2$ . This translates into a surface density  $\Sigma_{\text{cl}} \simeq 318 M_\odot \text{ pc}^{-2}$ . The velocity dispersion of a cloud of this size should be  $3.2 \text{ km/s} < \sigma_v < 4.2 \text{ km/s}$ ; we choose  $\sigma_{\text{turb}} = 3.6 \text{ km/s}$  to have the cloud supported against self-gravity (see below). For simplicity, we consider the cloud to be spherical with uniform density.

The gravitational binding energy of the cloud is

$$e_b \simeq \frac{3}{5} \frac{GM}{R} \simeq 2.5 \times 10^{11} M_5 R_{10}^{-1} \text{ erg g}^{-1}, \quad (2)$$

where  $M_5 = M/10^5 M_\odot$  and  $R_{10} = R/(10 \text{ pc})$ . The virial temperature of the cloud is  $T_{\text{vir}} \simeq 3800 M_5 R_{10}^{-1} \text{ K}$ , much higher than the typical gas temperature  $T \sim 10 \text{ K}$ . Support against rapid gravitational collapse comes from supersonic turbulence, with typical turbulent velocity dispersion

$$\sigma_{\text{turb}} \simeq \sqrt{\frac{3}{10} \frac{GM}{R}} \simeq 3.6 M_5^{1/2} R_{10}^{-1/2} \text{ km s}^{-1}. \quad (3)$$

The effective dynamical pressure of the cloud is

$$\frac{P_{\text{grav}}}{k_b} \simeq \frac{\rho \sigma_{\text{turb}}^2}{k_b} = n T_{\text{vir}} \simeq 1.4 \times 10^6 M_5^2 R_{10}^{-4} \text{ K cm}^{-3}. \quad (4)$$

Here,  $\rho \simeq 1.6 \times 10^{-21} M_5 R_{10}^{-3} \text{ g cm}^{-3}$  and  $n \simeq 380 M_5 R_{10}^{-3} \text{ cm}^{-3}$  are the mass density and particle density in the cloud, respectively.

From equation (4) we see that as long as the pressure in the ISM surrounding the cloud is  $P_{\text{ISM}}/k_b \ll 1.4 \times 10^6 \text{ K}$

$\text{cm}^{-3}$ , the cloud evolution is unaffected by external pressure. This is the case in most ‘normal’ environments, where  $P_{\text{ISM}}/k_b < 10^5 \text{ K cm}^{-3}$  (Wolfire et al. 2003). If the external pressure increases above this value, the cloud is compressed. The exact situation depends on the dynamics of the surrounding ISM.

##### 3.1.1 Negligible lateral velocity

In the simplest case, the external pressure around the molecular cloud increases isotropically and homogeneously. This is an unlikely scenario, since typically high pressure is caused by a shockwave enveloping the cloud. There are, however, a few situations where the velocity of the cloud with respect to its surroundings is low. First of all, the vertical gas velocity dispersion in gas-rich starburst galaxy discs can be as large as  $\sim 50 - 100 \text{ km/s}$  (Quinn et al. 1993; Scoville et al. 1997; Bryant & Scoville 1999), so it is conceivable for a given molecular cloud to be moving with a velocity  $> 100 \text{ km/s}$  vertically w.r.t. the rest frame of the galactic disc. A low-density ( $n_{\text{out}} \sim 0.1 - 1 \text{ cm}^{-3}$ ) outflow in the galactic halo moving with velocity  $v_{\text{out}} = 1000 \text{ km/s}$  produces a shockwave in the galactic disc (which has a density  $n_{\text{ISM}} \sim 10 - 100 \text{ cm}^{-3}$ ; c.f. Thompson et al. 2005; Abramova & Zasov 2008) with a velocity of order  $v \sim v_{\text{out}} (n_{\text{out}}/n_{\text{ISM}})^{1/2} \sim 100 \text{ km/s}$ . It is therefore possible that in the reference frame moving with the cloud, the shockwave is much slower than the sound speed of the shocked gas behind it. The direct interaction between the molecular cloud and the passing shockwave is mitigated by the atomic hydrogen envelope around the cloud (see also Section 6.6.2). In another case, a cloud that forms due to cooling of gas inside the fast hot outflow also experiences high external pressure without significant lateral motion.

The effect of this high isotropic pressure is to compress the cloud. In order to withstand this pressure, the cloud should have a higher turbulent velocity dispersion. We can update equation (3) to include external confinement:

$$\sigma'_{\text{turb}} \simeq \sqrt{\frac{3}{10} \frac{GM}{R} + \frac{P_{\text{ISM}}}{\rho_{\text{cl}}}}; \quad (5)$$

alternatively, one can express the updated velocity dispersion in terms of the pressure ratio:

$$\sigma'_{\text{turb}} = \sigma_{\text{turb}} \sqrt{1 + \frac{n_{\text{ISM}} T_{\text{ISM}}}{n T_{\text{vir}}}} \simeq 10.3 M_5^{-1/2} R_{10}^{3/2} P_7^{1/2} \text{ km/s}. \quad (6)$$

In this equation,  $n_{\text{ISM}}$  and  $T_{\text{ISM}}$  refer to the density and temperature of the confining hot phase ISM, respectively, and  $P_7 = P_{\text{ISM}}/(10^7 k_b \text{ K cm}^{-3})$ . We further assume that the ISM pressure is purely thermal. A corresponding timescale for the evolution of the compressed cloud, which we term the effective dynamical timescale, is

$$t'_{\text{dyn}} \sim t_{\text{dyn}} \frac{\sigma_{\text{turb}}}{\sigma'_{\text{turb}}} = t_{\text{dyn}} \left( 1 + \frac{n_{\text{ISM}} T_{\text{ISM}}}{n T_{\text{vir}}} \right)^{-1/2}, \quad (7)$$

where  $t_{\text{dyn}} \simeq 1.7 M_5^{-1/2} R_{10}^{3/2} \text{ Myr} \propto \sigma_{\text{turb}}^{-1}$  is the dynamical timescale of the cloud.

A shockwave is driven into the cloud approximately isotropically. It has a predominantly radial velocity (cf., e.g.,

Jog & Solomon 1992; Spitzer 1978)

$$v_{\text{sh}} \sim \left( \frac{P_{\text{ISM}}}{\rho_{\text{cl}}} \right)^{1/2} \sim \left( \frac{\rho_{\text{ISM}}}{\rho_{\text{cl}}} \right)^{1/2} c_{\text{s,ISM}} \sim \sigma'_{\text{turb}}, \quad (8)$$

where the last equality is valid if  $P_{\text{ISM}} \gg P_{\text{grav}}$ . The timescale for the shockwave to reach the centre of the cloud, known as the cloud crushing timescale (Klein et al. 1994), is the same as  $t'_{\text{dyn}}$  provided that  $P_{\text{ISM}} \gg P_{\text{grav}}$ . In the opposite case, the cloud crushing timescale becomes longer than dynamical and crushing is essentially negligible, as expected.

The passage of the shockwave heats the gas to temperatures

$$T_{\text{sh}} \sim \frac{3\mu_{\text{cl}}m_{\text{p}}}{16k_{\text{B}}}v_{\text{sh}}^2 \sim \frac{3}{16} \frac{\rho_{\text{ISM}}}{\rho_{\text{cl}}} T_{\text{ISM}}. \quad (9)$$

For an ISM pressure  $P_{\text{ISM}}/k_{\text{B}} = 10^7 \text{ K cm}^{-3}$ , this translates into a postshock temperature  $T_{\text{sh}} \sim 2 \times 10^3 \text{ K}$ . Using the postshock gas density  $n_{\text{sh}} = 4n_{\text{cl}}$  (strong shock approximation; we further assume that gas remains mostly molecular in the shock, since the temperature increase is not enough to completely dissociate  $\text{H}_2$  or  $\text{CO}$ ) and the cooling function approximation from McKee & Cowie (1977, Table 1), we find the gas cooling time  $t_{\text{cool}} \sim 400 \text{ yr} \ll t'_{\text{dyn}}$ . Therefore the postshock gas can be assumed to cool instantaneously and attain a density (cf. Jog & Solomon 1992)

$$n_{\text{final}} \simeq \frac{16}{3} \frac{T_{\text{sh}}}{T_{\text{vir}}} n_{\text{cl}} \simeq \frac{P_{\text{ISM}}}{P_{\text{grav}}} n_{\text{cl}} \simeq 2.7 \times 10^3 P_7 M_5^{-1} R_{10} \text{ cm}^{-3}. \quad (10)$$

This final density increase by  $\sim 7$  times over the mean cloud density lowers the Jeans' length and mass of the post-shock gas by a factor  $\sim 2.6$ , assuming that the temperature stays the same. This means that smaller density perturbations become unstable and collapse to form stars, leading to rapid star formation in the shell driven into the cloud.

If the cloud forms under conditions of high external pressure, its turbulent velocity should have a value as given by equation (6). Such a cloud would not be bound by its own gravity, but as long as the external pressure persists, it is able to fragment and form stars. The timescale of the cloud evolution is  $R/\sigma'_{\text{turb}} = t'_{\text{dyn}}$ . Only a weak shockwave is driven into the cloud, so star formation starts in the central parts of the cloud, where the local dynamical time is shortest.

### 3.1.2 Large lateral velocity

If the cloud is compressed by a passage of a shockwave, such that the shear velocity  $v_{\text{lat}}$  of the postshock ISM gas with respect to the cloud is significant compared with the sound speed in this gas, the shear affects the cloud evolution. Direct interaction between a strong shock and the GMC is unlikely to occur: GMCs are typically surrounded by warm atomic hydrogen envelopes, which slow down and weaken the shockwave. The shockwave driven into the cloud is no longer approximately spherical. In the leading edge of the cloud, the shockwave velocity is approximately

$$v_{\text{sh,lat}} \sim \left( \frac{\rho_{\text{ISM}}}{\rho_{\text{cl}}} \right)^{1/2} (c_{\text{s,ISM}}^2 + v_{\text{lat}}^2)^{1/2}. \quad (11)$$

In other directions, the velocity is lower than this, but never lower than  $v_{\text{sh}}$  (eq. 8). The cloud is destroyed by the shock-

wave on a timescale

$$t_{\text{destr}} \sim A \frac{R}{v_{\text{lat}}} \left( \frac{\rho_{\text{ISM}}}{\rho_{\text{cl}}} \right)^{-1/2}, \quad (12)$$

where  $A$  is a factor of order a few (Klein et al. 1994; Agertz et al. 2007, finds  $A \simeq 1.6$ ). The sound speed of the hot ISM does not enter into the expression for the cloud destruction timescale because cloud compression happens isotropically and does not disperse the cloud. We can use this expression together with the effective dynamical time  $R/v_{\text{sh,lat}}$  to estimate the mass of stars that form in a cloud thus affected:

$$\begin{aligned} M_{*,\text{lat}} &\sim \epsilon_{*,\text{ff}} M \frac{t_{\text{destr}} v_{\text{sh,lat}}}{R} \\ &\sim A \epsilon_{*,\text{ff}} M \frac{(c_{\text{s,ISM}}^2 + v_{\text{lat}}^2)^{1/2}}{v_{\text{lat}}} \geq A \epsilon_{*,\text{ff}} M. \end{aligned} \quad (13)$$

The net result is that even though the cloud is destroyed by the shear, the mass of stars formed from the cloud is larger than in a free-floating cloud. In a particular case of a strong shock and stationary cloud, where  $c_{\text{s,ISM}}^2/v_{\text{lat}}^2 = 5$ , this ratio is  $\sim 2.5A$  and the fraction of mass converted into stars can exceed 10% before the cloud disperses.

## 3.2 Cluster survival in high-pressure systems

The low integrated (that is, calculated over the lifetime of the cloud rather than its dynamical time) efficiency of mass conversion into stars in a GMC suggests that the clouds are rapidly destroyed by stellar feedback. It is not well understood which of the many feedback processes are most important. It has been recently proposed that massive star clusters can form in molecular clouds that have escape velocities higher than the sound speed in ionized gas  $c_{\text{HII}} \sim 10 \text{ km/s}$  (Bressert et al. 2012). For unconfined clouds, this condition translates to a critical mass  $M_{\text{crit}} \sim 7 \times 10^6 M_{\odot}$ ; clouds above this mass retain even photoionized gas (Kroupa & Boily 2002; Krumholz & Matzner 2009). If no other feedback processes were relevant, this would lead to such massive clouds having star formation efficiencies of several times 10%. On the other hand, these massive clouds may be destroyed by radiation pressure (Krumholz & Matzner 2009; Fall et al. 2010; Murray et al. 2010) and thus maintain a low integrated star formation efficiency. It is, however, not clear how important radiation pressure feedback is (Krumholz & Thompson 2012, 2013).

No matter which feedback process disrupts the cloud, it must counteract the forces holding the cloud together. For a free-floating cloud, the only such force is the self-gravity of the cloud. Within our model, external pressure acts as an additional factor preventing gas escape and cloud dispersal. In the case of photoionization, the cloud is unable to expand and disperse provided that the total confining pressure (produced by both cloud self-gravity and ambient ISM) is higher than  $P_{\text{crit}} \simeq \rho_{\text{cl}} c_{\text{HII}}^2 = 1.6 \times 10^{-9} M_5 R_{10}^{-3} \text{ erg cm}^{-3}$ . For our fiducial cloud parameters, this translates into a required ISM pressure

$$P_{\text{ISM}} = \rho_{\text{cl}} (c_{\text{HII}}^2 - \sigma_{\text{turb}}^2) \simeq 1.4 \times 10^{-9} \text{ erg cm}^{-3}, \quad (14)$$

or, equivalently

$$\frac{P_{\text{ISM}}}{k_{\text{B}}} = 9.9 \times 10^6 \text{ K cm}^{-3}. \quad (15)$$

The balance between photoionization heating and stellar winds on one side and external pressure on the other allows the cloud to survive the photoionizing radiation of young stars. Similar estimates based on pressure balance can be made for other forms of feedback, but these are beyond the scope of this paper. We merely wish to point out that as a result of external pressure, the cloud survives for longer against feedback than if it were not compressed. Therefore, the integrated star formation efficiency  $M_*/M_{\text{cl}}$  is higher than in unconfined clouds even if the star formation efficiency per dynamical time ( $\epsilon_{\text{ff},*}$ ) were the same. Even small clouds can have large SFEs, giving rise to more strongly bound clusters. A similar result was found by Elmegreen & Efremov (1997), who suggested that high external pressure reduces mass loss from nascent globular clusters and so enhances their survival prospects.

### 3.3 Summary

The calculations above reveal three major effects that confining external pressure has on a molecular cloud:

(i) The cloud is compressed, reducing the effective dynamical timescale and thus increasing the rates of fragmentation and star formation. This should be a general effect of higher ambient pressure, independent of its source, the timescale over which the pressure increases or the shear velocity of the hot ISM w.r.t. the cloud.

(ii) A shockwave is driven into the cloud from the sides toward the centre; the density in the postshock region exceeds that of the undisturbed cloud medium by a factor  $\sim 7$ , facilitating star formation there. As a result, stars form more rapidly in compressed clouds than in undisturbed ones, so that the cloud evolves on the effective dynamical timescale. The shockwave is approximately spherical if the lateral motion of the ISM past the cloud is slow. If this velocity is large, the cloud is destroyed by the shockwave in a few effective dynamical times. The presence of the shockwave is guaranteed only if the external pressure increases around the cloud on a timescale shorter than the cloud dynamical time; otherwise, the cloud has time to establish virial equilibrium with the higher surrounding pressure.

(iii) As long as the total (external plus gravitational) pressure confining the cloud exceeds the pressure created by stellar feedback, the cloud is not disrupted and can continue to form stars. For the case of photoionizing feedback, this pressure is  $\sim 1.6 \times 10^{-9} M_5 R_{10}^{-3} \text{ erg cm}^{-3}$ , easily reached in ISM heated by supernovae or AGN activity. The fraction of gas converted into stars is larger in confined clouds than in uncompressed ones, leading to formation of more tightly bound clusters.

Although these conclusions seem robust based on analytical calculations alone, we wish to investigate the evolution of compressed clouds in more detail. Therefore, we turn to numerical simulations.

## 4 NUMERICAL SIMULATIONS

We run a number of simulations using the hybrid N-body/SPH code GADGET-3 (an updated version of the publicly available code from Springel 2005). We utilize the

SPHS method (Read & Hayfield 2012), which is specifically designed to remove artificial conductivity errors in standard SPH and resolve mixing of multiphase material (Read et al. 2010) and had been used successfully in modelling multiphase flows (Hobbs et al. 2013). We employ the fourth-order HOCT4 kernel with 442 neighbours, and use adaptive smoothing and gravitational softening lengths.

Each model starts with a spherically symmetric cloud with  $M_{\text{cl}} = 10^5 M_{\odot}$  and  $R_{\text{cl}} = 10 \text{ pc}$ , giving a mean particle density of molecular hydrogen  $n_{\text{cl}} \simeq 380 \text{ cm}^{-3}$ . We assume the cloud to have uniform density initially; we comment on this assumption in the Discussion (Section 6.6.2). The dynamical time of the cloud is  $t_{\text{dyn}} \simeq 1.7 \text{ Myr}$ . The cloud is supported against self-gravity by a large-scale turbulent velocity field with a characteristic velocity  $\sigma_{\text{turb}}$ .

We choose an implementation of turbulent velocities that produces a purely solenoidal (divergence-free) turbulent velocity spectrum (Dubinski et al. 1995; Hobbs et al. 2011). This means that turbulence is incompressible; another extreme would be a purely compressive (curl-free) turbulence. Although supersonic turbulence is generally at least partially compressive, a large fraction of the turbulent energy is expected to be in solenoidal modes (Federrath et al. 2010; Hennebelle & Falgarone 2012), so we are confident that our choice of the velocity spectrum is not totally unrealistic. Furthermore, solenoidal turbulence has a shallower power spectrum than compressive one. Numerical simulations tend to steepen the spectrum as time goes by, since turbulence decays artificially starting from the smallest length scales (highest wavenumbers), therefore our choice of turbulent power spectrum should produce more realistic results than the opposite extreme. Finally, it is important to note that density perturbations grow  $\sim 10$  times slower for solenoidal turbulence than with purely compressive turbulence (Federrath et al. 2010), thus our results of fragmentation rates are most likely underestimates.

From a technical point of view, turbulence is implemented as follows. The velocity field has a Kolmogorov power spectrum

$$P_v(k) \propto k^{-11/3}, \quad (16)$$

where  $k$  is the wavenumber. The velocity can be described as a curl of a vector potential  $A$  (this means that the velocity field is homogeneous and incompressible) and so the power spectrum can be expressed as

$$\langle |A_k|^2 \rangle = C (k^2 + k_{\text{min}}^2)^{-17/6}, \quad (17)$$

where  $k_{\text{min}} \simeq R_{\text{cl}}^{-1}$  is the minimum wavelength of turbulence and  $C$  is an arbitrary constant which is set later in order to give the characteristic velocity  $\sigma_{\text{turb}}$ . The vector potential is sampled in Fourier space on a periodic cubic grid of  $256^3$  cells, calculating the value of  $A_k$  using eq. (17). The curl of  $A_k$  then gives the velocity field in Fourier space, which is Fourier-transformed into real space. We then use tricubic interpolation to calculate the velocity of each SPH particle.

Once the turbulent velocities are set up, we scale them to give the desired characteristic velocity (and hence turbulent energy). We consider two values of  $\sigma_{\text{turb}}$ . The lower value,  $\sigma_{\text{turb}} = 4 \text{ km/s}$ , supports the cloud against self gravity and creates a dynamical pressure inside the cloud  $P_{\text{dyn}}/k_b \simeq 1.7 \times 10^6 \text{ K cm}^{-3}$ . The higher value,  $\sigma_{\text{turb}} = 10 \text{ km/s}$ , creates the same dynamical pressure as a cloud filled with pho-

Model ID	$v_{\text{turb}}$ (km/s)	$T_{\text{ISM}}$ (K)	$\Omega_{\text{rot}}$ (km/s/pc)	$v_{\text{lat}}$ (km/s)	$t_{\text{sink}}$ (Myr)	$t_{\text{frag}}$ (Myr)	$r_{\text{h}}$ (pc)	$\epsilon_{\text{ff,sink}}$
t4T5	4	$10^5$	0	0	1.26	1.78	4.26	0.076
t4T7	4	$10^7$	0	0	0.37	0.43	1.37	> 0.9*
t10T5	10	$10^5$	0	0	1.51	2.51	8.29	0.016
t10T7	10	$10^7$	0	0	0.40	0.56	1.68	> 0.9*
t2.8r4.2T5	2.8	$10^5$	0.42	0	1.33	1.98	3.81	0.036
t2.8r4.2T7	2.8	$10^7$	0.42	0	0.34	0.42	1.04	0.75
t4v10T5	4	$10^5$	0	10	1.33	1.66	2.68	0.28
t4v10T7	4	$10^7$	0	10	0.36	0.42	1.30	0.98
t4v30T5	4	$10^5$	0	30	1.33	1.66	2.80	0.27
t4v30T7	4	$10^7$	0	30	0.36	0.42	1.30	0.96
t4v100T5	4	$10^5$	0	100	1.23	1.59	2.94	0.43
t4v100T7	4	$10^7$	0	100	0.29	0.43	2.25	0.92
t4v300T5	4	$10^5$	0	300	1.08	1.39	3.85	0.52
t4v300T7	4	$10^7$	0	300	0.60	0.89	1.48	0.80

**Table 1.** Parameters of the numerical models and most important results. The first column shows the model ID. The next four columns give the parameters: cloud turbulent velocity, confining ISM temperature, angular velocity of cloud rotation and linear velocity of shearing cloud motion, respectively. The final three columns are the primary results: time of formation of the first sink particles  $t_{\text{sink}}$ , fragmentation timescale  $t_{\text{frag}}$ , half mass radius  $r_{\text{h}}$  at fragmentation time and efficiency of gas conversion into sink particles in one dynamical time  $\epsilon_{\text{ff,sink}}$ . Numbers with asterisks are extrapolated from earlier snapshots.

toionised gas would have:  $P_{\text{dyn}}/k_{\text{b}} \simeq 1.06 \times 10^7 \text{ K cm}^{-3}$ . We choose to represent photoionized gas with a higher turbulent velocity, rather than higher gas temperature, because photoionization predominantly affects diffuse gas (Dale & Bonnell 2011) and does not necessarily stop the collapse of already dense regions (Dale et al. 2012); turbulence mimics this behaviour better than a uniform increase in gas internal energy. Alternatively, the large value of turbulence may represent a cloud which forms within a high-pressure outflow (Zubovas & King 2014).

The cloud is surrounded by an ISM with particle density  $n_{\text{ISM}} = 1 \text{ cm}^{-3}$  and temperature of either  $10^5 \text{ K}$  or  $10^7 \text{ K}$ . This produces a pressure either much lower than the dynamical pressure of the cloud ( $P_{\text{ISM}}/k_{\text{b}} = 10^5 \text{ K cm}^{-3}$ ) or pressure high enough to confine even the highly turbulent cloud ( $P_{\text{ISM}}/k_{\text{b}} = 10^7 \text{ K cm}^{-3}$ ). Accordingly, the models are called “uncompressed” and “compressed” respectively. The high external pressure is also higher than the ISM pressure necessary to prevent cloud dispersal by photoionization (see eq. 14). The whole system is set up in a periodic box of side length 80 pc (models with shearing motion use a box of side length 160 pc).

All the models use the same number of particles,  $N = 10^6$ , to represent the cloud, giving a mass resolution  $m_{\text{res}} = 442m_{\text{SPH}} = 44.2 \text{ M}_{\odot}$ . This resolution is good enough to resolve very massive stars and small stellar associations. We implement a cooling function appropriate for dense gas at temperatures between 10 and  $10^4 \text{ K}$  (Inoue & Inutsuka 2008), which we modify so that cooling is turned off for gas at temperatures between  $3 \times 10^4 \text{ K}$  and  $T_{\text{ISM}}$ . With this prescription, the cloud gas is modelled with reasonable accuracy, while the surrounding ISM stays isothermal.

In order to speed up simulations and track the fragmentation within the cloud, we introduce sink particles in regions where the density exceeds  $\rho_{\text{crit}} = 10^{-17} \text{ g cm}^{-3} \simeq 1.5 \times 10^5 \text{ M}_{\odot} \text{ pc}^{-3}$ . At temperature  $T = 10 \text{ K}$ , this corresponds to a Jeans’ mass  $M_{\text{J}} \simeq 0.4 \text{ M}_{\odot} = 4m_{\text{SPH}}$ . This mass is similar to that of pre-stellar cores, so our simulations should not overproduce the number and total mass of

fragments. The low Jeans’ mass allow us to track gas dynamics down to the resolution limit and below (albeit with lower accuracy below  $\sim 40 \text{ M}_{\odot}$ ).

The models analysed are listed in Table 1. We first consider models with zero lateral velocity - t4T5, t4T7, t10T5, t10T7, t2.8T5r4.2 and t2.8T7r4.2, where each model is labelled by the value of turbulence (“t”, in km/s), logarithm of surrounding ISM pressure (“T”) and rotational velocity at the edge of the cloud (“r”, in km/s). These simulations are designed to show the basic behaviour of clouds compressed by the hot ISM. Next, we model the more realistic cases of non-zero shear, with relative velocities of the ISM w.r.t the cloud (“v”) of 10, 30, 100 and 300 km/s. The duration for which we run each simulation is determined by numerical resources, but in all cases, by the end of the simulation at least 70% of the cloud gas is converted into sink particles.

## 5 RESULTS

We divide the result presentation into two parts. First we analyze the effects of external pressure without shear, including cases of static gravitationally bound clouds (models t4T5 and t4T7), static gravitationally unbound clouds (models t10T5 and t10T7) and rotating gravitationally bound clouds (t2.8T5r4.2 and t2.8T7r4.2). Next, we consider the effects of progressively stronger shear upon self-gravitating clouds (models t4vXT5 and t4vXT7).

For each model, we derive four parameters which allow for easy quantitative comparison of their progress. The first parameter is the time when the first sink particle forms, which we use as a proxy for the onset of star formation. Secondly, we define the fragmentation time,  $t_{\text{frag}}$ , as the time when the sink particle mass fraction reaches 20%; the choice of the particular mass fraction is arbitrary, but choosing either 10% or 30% does not affect our conclusions. The third parameter is the half-mass radius of the system,  $r_{\text{h}}$ , at  $t = t_{\text{frag}}$ . Finally, we define the efficiency of sink particle formation  $\epsilon_{\text{ff,sink}}$  as the mass fraction of sink particles

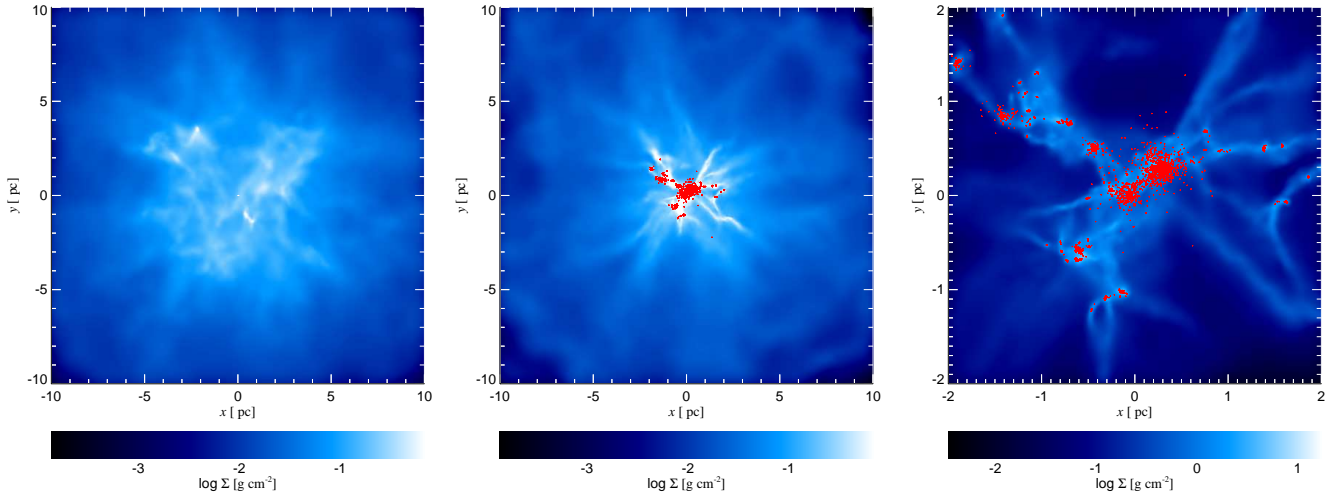


**Figure 1.** Evolution of the uncompressed cloud model, t4T5. **Left panel:**  $t = 1.26$  Myr, just before the first sink particles appear; the cloud initially expands slightly and develops an uneven density structure due to turbulence, with higher density in the centre and several high-density blobs and filaments. **Middle panel:**  $t = 1.78$  Myr, when  $M_{\text{sink}} = 0.2 (M_{\text{cl}} + M_{\text{sink}})$ ; sink particles form predominantly in the centre of the cloud, where the dynamical time is shortest and densities are highest. **Right panel:** zoom in to the centre of the cloud at  $t = 1.78$  Myr; sink particles have formed in several clumps where turbulent motions created overdense regions. Note the density scale change in this panel compared with the previous two. In the last panel, only 10% of sink particles are shown for clarity.

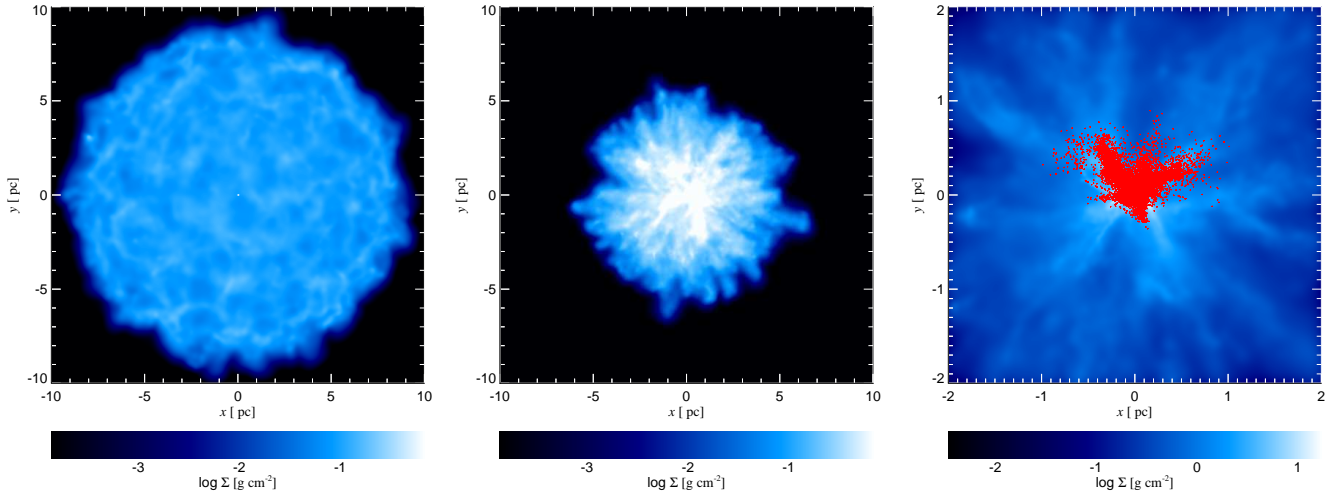


**Figure 2.** Evolution of the compressed cloud model, t4T7. **Left panel:**  $t = 0.14$  Myr; the cloud is confined and slowly compressed by the surrounding medium, developing an overdense shell at the interface. **Middle panel:**  $t = 0.37$  Myr, just before the first sink particles appear; the cloud radius is decreasing, but Richtmyer-Meshkov instabilities destroy a coherent shockwave. **Right panel:**  $t = 0.43$  Myr, when  $M_{\text{sink}} = 0.2 (M_{\text{cl}} + M_{\text{sink}})$ ; sink particles are forming vigorously in a single clump in the centre of the cloud. Note the density and size scale change in this panel compared with the previous two. In the last panel, only 10% of sink particles are shown for clarity.

after one dynamical time of the cloud, i.e. 1.7 Myr. The numerical values of these parameters are given in the last three columns of Table 1. The error due to time resolution of the simulations is  $\pm 0.02$  Myr, while fractional errors on distances are  $\pm 0.02$ .

## 5.1 Models with no shear

### 5.1.1 Triggering of fragmentation

Figures 1 and 2 show the column density plots which depict the evolution of the models t4T5 and t4T7, respectively. The uncompressed model quickly develops an uneven density structure and expands slightly, before starting to collapse as the turbulence decays. The density increases mainly in the central parts of the cloud, which develop an isothermal ( $\rho \propto R^{-2}$ ) density structure (left panel, also Figure 3, left panel). Star formation begins in the central regions,

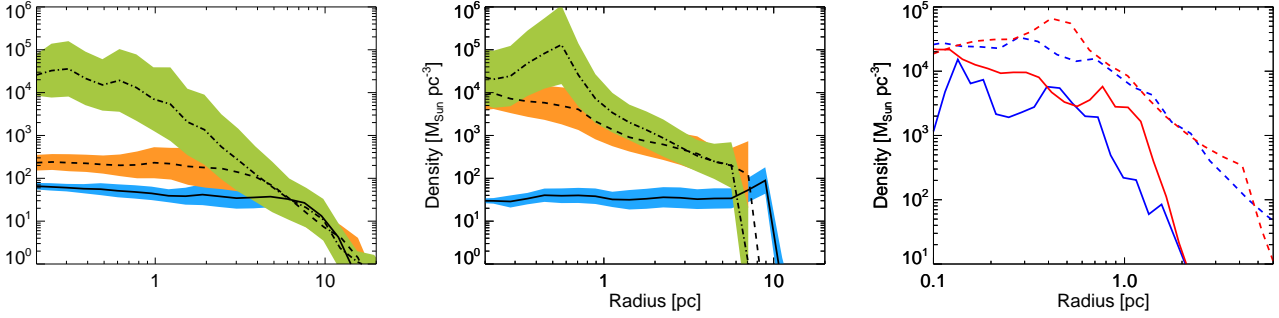


**Figure 3.** Radial density profiles. **Left panel:** model t4T5 at 0.47, 1.26 and 1.78 Myr (solid, dashed and dot-dashed lines, respectively; each line is created by averaging the values of three subsequent snapshots, in order to reduce numerical noise). Coloured regions indicate  $\pm 1\sigma$  deviation from the mean of  $\log \rho$ . The cloud develops an approximately isothermal density profile, and its density exceeds the star formation threshold only in the very centre. **Middle panel:** model t4T7 at 0.14, 0.37 and 0.43 Myr. Line styles and colours as in previous panel. The cloud is compressed, with a weak shockwave (density ratio  $\sim 2$ ) moving inward. The threshold density for star formation is still reached only in the centre. **Right panel:** sink particle radial profiles (solid lines) and gas radial profiles (dashed lines) at  $t = t_{\text{frag}}$ : blue lines indicate t4T5, red lines indicate t4T7. The gas density profiles are identical except for the presence of a shockwave in model t4T7, while the sink particles in t4T7 are distributed slightly more widely than in the uncompressed model.

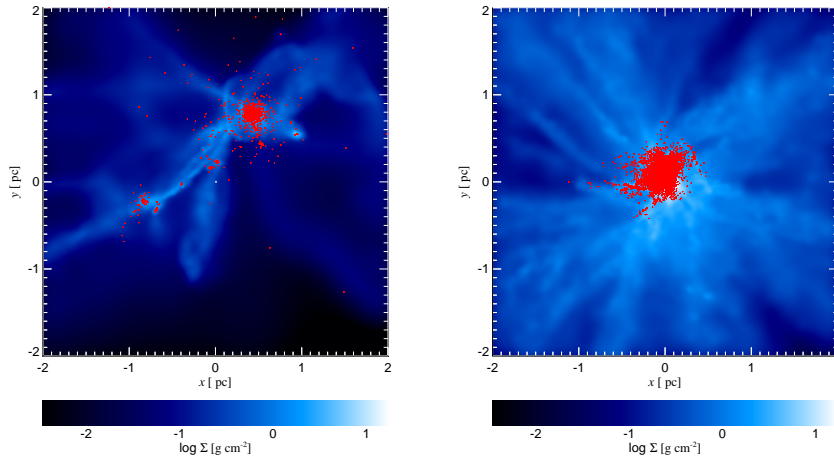


**Figure 4.** Morphology of the two high turbulence models, t10T5 (left panel) and t10T7 (right panel), when the sink particle mass fraction is 20%. This happens at  $t = 2.51$  Myr for the uncompressed model and at  $t = 0.56$  Myr for the compressed cloud. Even high turbulence is unable to prevent confinement and collapse of the cloud embedded in a high-pressure hot ISM. Only 10% of sink particles are shown for clarity.

where the density is highest due to convergent turbulent flows. Sink particles form along filaments and are gradually absorbed into a central elliptical cluster (right panel). The fraction of mass converted into sink particles in one dynamical time of the cloud is  $\epsilon_{\text{ff},\text{sink}} \simeq 7\%$ . Multiplying this value by the single-core star formation efficiency of 25–75% (Matzner & McKee 2000; Alves et al. 2007) gives a star formation efficiency  $\epsilon_{\text{ff},*} \simeq 2 - 5\%$ . The similarity of this result to the observationally derived value (McKee & Ostriker 2007) is partly coincidental, and depends sensitively on the initial conditions, especially the characteristic turbulent velocity of the cloud (Bate et al. 2003). Furthermore, the decay of turbulence in the cloud is partly responsible for the high fragmentation rate (see Section 6.6.3).

The evolution of the compressed cloud is notably dif-

ferent in two aspects. As expected, the hot ISM confines the cloud and compresses it (Figure 2, left panel and Figure 3, middle panel). However, there is no clearly visible shockwave moving inward through the cloud. This happens because Richtmeier-Meshkov (RM) instabilities begin growing along the interface between the cloud and the ISM on a timescale comparable to the cloud crushing timescale (Klein et al. 1994). These instabilities manifest as thick fingers visible in the middle panel of Figure 2. The first sink particles appear at  $t \sim 0.37$  Myr. Much like in the uncompressed model, they form in the centre of the cloud, where growing instabilities increase mixing rate and promote the formation of high-density clumps. Unlike the uncompressed model, however, the sink particles are more likely to escape their parent clumps, so the mean mass of sink particles is



lower, and all sink particles form a single large cluster, rather than keeping a complex substructure. All of the cloud gas is converted into sink particles well before 1.7 Myr, giving a formal fragmentation efficiency  $\epsilon_{\text{ff},\text{sink}} > 100\%$ .

We compare the radial density profiles of gas (dashed lines) and sink particles (solid lines) in the two models at  $t = t_{\text{frag}}$  in the right panel of Figure 3. The gas density profiles are almost identical in the two models, except for a weak shockwave (density ratio  $\sim 2$ ) in model t4T7 (red line) at  $0.3 \text{ pc} < R < 0.7 \text{ pc}$ . Both gas density profiles are slightly steeper than isothermal,  $\rho \propto R^{-2.5}$ , outside  $R \simeq 0.7 \text{ pc}$ . They should flatten over time. The sink particles are slightly more centrally concentrated than the gas in both models; furthermore, the uncompressed cloud has a smaller “core” of sink particles, going out to  $\sim 0.5 \text{ pc}$ , as opposed to the  $\sim 1 \text{ pc}$ -wide core in the compressed model. The outer slopes of sink particle density profiles are very steep in both models,  $d \ln \rho / d \ln R \simeq -4$ – $-5$ , which should later expand and relax to a shallower distribution.

The morphology of high turbulence models, t10T5 and t10T7, is presented in Figure 4. The unconfined cloud expands significantly, with some filaments reaching radii of  $> 30 \text{ pc}$ . Meanwhile, the density in the central parts keeps increasing and the first sink particles appear at 1.51 Myr, not much later than in the low turbulence model (t4T5, 1.26 Myr). Later on, however, the fragmentation rate stays much lower than in t4T5 (see Section 5.1.3). As a result, the fragmentation efficiency is only  $\epsilon_{\text{ff},\text{sink}} \simeq 1.6\%$ . This is much lower than the 5–10% found by Clark et al. (2005), presumably because those authors considered a cloud with  $E_{\text{turb}}/E_{\text{grav}} = 2$ , whereas in our model, the ratio is 7.7. The sink particle cluster that eventually forms in the central parts (Figure 4, left panel) is not a realistic result due to the decay of turbulence (see Section 6.6.3) and lack of stellar feedback (see Section 6.3), which would presumably destroy the cloud.

The confined highly turbulent cloud (Figure 4, right panel) evolves in a very similar way to its low turbulence analogue. The cloud expands very little at first, but is quickly confined and compressed; even though the shockwave is weak, RM instabilities form behind it and help increase gas density, which leads to formation of the first sink particles at  $t \simeq 0.40 \text{ Myr}$ , a very similar time to model t4T7. Subsequently, both the fragmentation rate and fragment mass fraction increase exponentially, with 20% sink particle mass fraction achieved by  $t_{\text{frag}} = 0.56 \text{ Myr}$  (compare with  $t_{\text{frag}} = 0.43 \text{ Myr}$  of t4T7). The half-mass radius of the cloud is slightly larger than in the model t4T7, but this difference does not affect the global evolution: just as in t4T7, all of the cloud gas turns into sink particles within one dynamical time.

These results show that the surrounding hot ISM pressure can have a dominant effect on molecular cloud evolution, provided it is larger than the dynamical pressure of the cloud. The affected cloud is confined, preventing gas dispersal (and reducing its tidal radius; see Section 6.3); a shockwave is driven into the cloud, followed by RM instabilities, which accelerate and trigger fragmentation.

### 5.1.2 Fragmentation of rotating clouds

We run two simulations, t2.8r4.2T5 and t2.8r4.2T7 (see Table 1), to investigate the effects of cloud rotation. The cloud is set up to have solid-body rotation around the Z axis with an angular velocity of  $\omega_{\text{rot}} = 0.42 \text{ km s}^{-1} \text{ pc}^{-1}$ . The characteristic turbulent velocity is reduced to  $2.8 \text{ km s}^{-1}$ . This ensures that the contributions to dynamical pressure from rotation and turbulence are approximately the same in the XY plane and that the total kinetic energy of the cloud is the same as in t4 models.

Even though the cloud rotation is slow, with  $\omega_{\text{rot}} t_{\text{dyn}} \simeq 0.7$ , the uncompressed cloud evolves rather differently from the non-rotating case. The first two panels of Figure 5 show the cloud morphology at  $t = t_{\text{frag}} = 1.98 \text{ Myr}$ . The cloud collapses vertically, forming a disc partially supported by rotation, which then fragments and starts producing sink particles in small clusters throughout the disc. The mean density of the gas disc is lower than of a spherically collapsing cloud, so the sink particles begin appearing slightly later, after  $\sim 1.33 \text{ Myr}$ . The fragmentation efficiency is accordingly lower,  $\epsilon_{\text{ff},\text{sink}} = 3.6\%$ .

Since the compressed rotating model evolves much faster, rotation does not have time to break the cloud into separate clumps. However, rotation has another important effect; the RM fingers that significantly affect the cloud evolution in the non-rotating models are sheared away, and the central parts of the cloud are effectively shielded from the shockwave. As a result, the highest densities are achieved at the edge of the cloud; this is also where most sink particles form (third panel of Figure 5). In the vertical direction, the cloud is strongly compressed (fourth panel of Figure 5), but the shockwave does not produce large enough densities for rapid fragmentation. It is interesting that the global parameters of cloud fragmentation are very similar to those of the non-rotating compressed model. The first sink particles appear after  $\sim 0.34 \text{ Myr}$  and  $t_{\text{frag}} = 0.42$ , leading to a large fragmentation efficiency  $\epsilon_{\text{ff},\text{sink}} = 75\%$ ; all these numbers are very similar to those of model t4T7.

### 5.1.3 Reduced effective dynamical time

Figure 6 shows the mass fraction of sink particles (solid lines) and fragmentation rate in Solar masses per year (dashed lines) for the six models described above (left panel - t4, middle panel - t10, right panel - t2.8r4.2 blue lines - T5, red lines - T7). The horizontal axis is scaled to the fragmentation timescale  $t_{\text{frag}}$  (see Table 1 and the beginning of this Section).

We see immediately that the time evolution of compressed and uncompressed models is qualitatively different. Model t4T7 (left panel, red lines) forms stars  $\sim 10$  times more rapidly than model t4T5, so even when scaled to the fragmentation timescale  $t_{\text{frag}}$ , the growth of sink mass fraction is much faster in the compressed cloud. Similar differences appear in the high-turbulence and rotating models.

It is interesting to compare the ratio of certain timescales for both models with analytical predictions. The analytical prediction for the effective dynamical time (Section 3.1.1 and eq. 7) is  $t_{\text{dyn}}/t'_{\text{dyn}} \simeq (P_{\text{ISM}} + P_{\text{grav}}/P_{\text{grav}})^{1/2} \simeq 2.9$ . The ratio of the times for the first sinks to form,  $1.26/0.37 \simeq 3.4$ , is similar, but somewhat

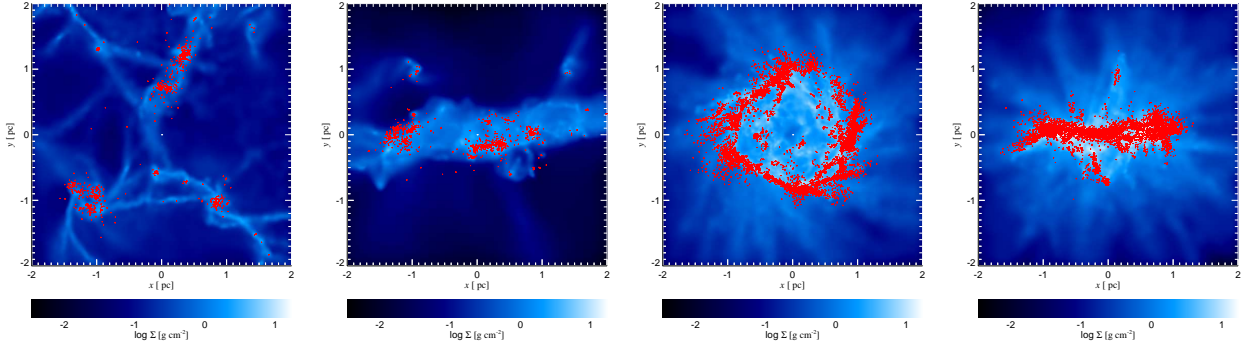


**Figure 5.** Morphology of rotating cloud models, t2.0r4.2T5 at  $t = 2.03$  Myr (two left panels) and t2.8r4.2T7 at 0.42 Myr (two right panels). First and third panels show the top-down view of the XY plane, second and fourth panels show the side view of the XZ plane. Rotation has a noticeable effect on the morphology of both uncompressed and compressed clouds, distributing the gas in a larger volume and preventing instability growth. Only 10% of sink particles are shown for clarity.

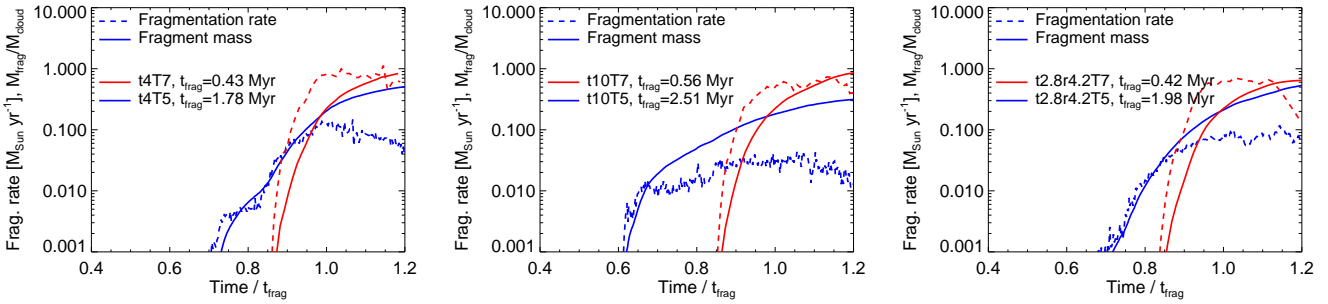


**Figure 6.** Fragmentation rates and growth of the sink particle population for the low turbulence (left panel), high turbulence (middle panel) and rotating (right panel) models. The time axis is scaled to the fragmentation timescale  $t_{\text{frag}}$  (see Table 1). In all three cases, compressed clouds show qualitatively faster fragmentation, with a much shorter time between first sink particles appearing and  $t_{\text{frag}}$  and a 10 – 20 times larger fragmentation rate. The compressed models evolve similarly independently of characteristic turbulent velocity or rotation.

larger. The discrepancy is even greater when we consider the fragmentation timescales:  $t_{\text{frag},t4T5}/t_{\text{frag},t4T7} = 1.78/0.43 \simeq 4.1$ . We see that the compressed cloud evolves progressively faster than the analytical estimate predicts. This accelerated fragmentation cannot be the result of increased mean cloud density, because both models have the same density profiles at  $t_{\text{frag}}$  (Figure 3, right panel). A possible explanation is the action of RM instabilities, which create denser and more diffuse regions while keeping the radial density profile the same. This facilitates the fragmentation of gas into sink particles. We tested this hypothesis by running these two simulations with the standard SPH formalism, where artificial surface tension suppresses instability growth, and found that the compressed cloud there evolves consistently with the analytical prediction.

The difference in evolution between the two high turbulence models is even larger. As expected, the uncompressed high-turbulence cloud, model t10T5, fragments very slowly, reaching only  $\dot{M}_{\text{frag}} \sim 0.04 M_{\odot} \text{ yr}^{-1}$  and maintaining this value for a long time, as turbulence decays and material gradually accumulates back in the centre of the cloud. The compressed cloud, however, evolves almost identically to its low-turbulence counterpart, exhibiting similar peak fragmentation rate and the ratio of  $t_{\text{frag}}$  to the time of the formation of the first sinks.

Both rotating models evolve in a similar way to the t4 models. Rotation slows down fragmentation in the uncompressed model, but otherwise the time evolution is almost identical. This is striking when considering how different the morphologies of the rotating and non-rotating compressed models are. Such similarity suggests that RM instabilities only increase the stratification of densities in the cloud, rather than compacting the cloud as a whole. In the rotating model, instabilities are confined to the outskirts of the cloud, but their effects still manifest.

Overall, the time evolution reveals that external compression enhances molecular cloud fragmentation in two ways. First of all, it pushes the cloud together, reducing the effective dynamical time. In addition, the shockwave generated by the high pressure ISM facilitates the formation of instabilities, which stratify gas density in some regions, accelerating fragmentation. Finally, if the cloud is confined by external pressure, the characteristic turbulent velocity has very little effect on the cloud evolution.

## 5.2 Cloud with shearing motion

We perform eight simulations of clouds moving with respect to the surrounding ISM (see Table 1) to evaluate the effects of progressively stronger shearing motion. The low-pressure

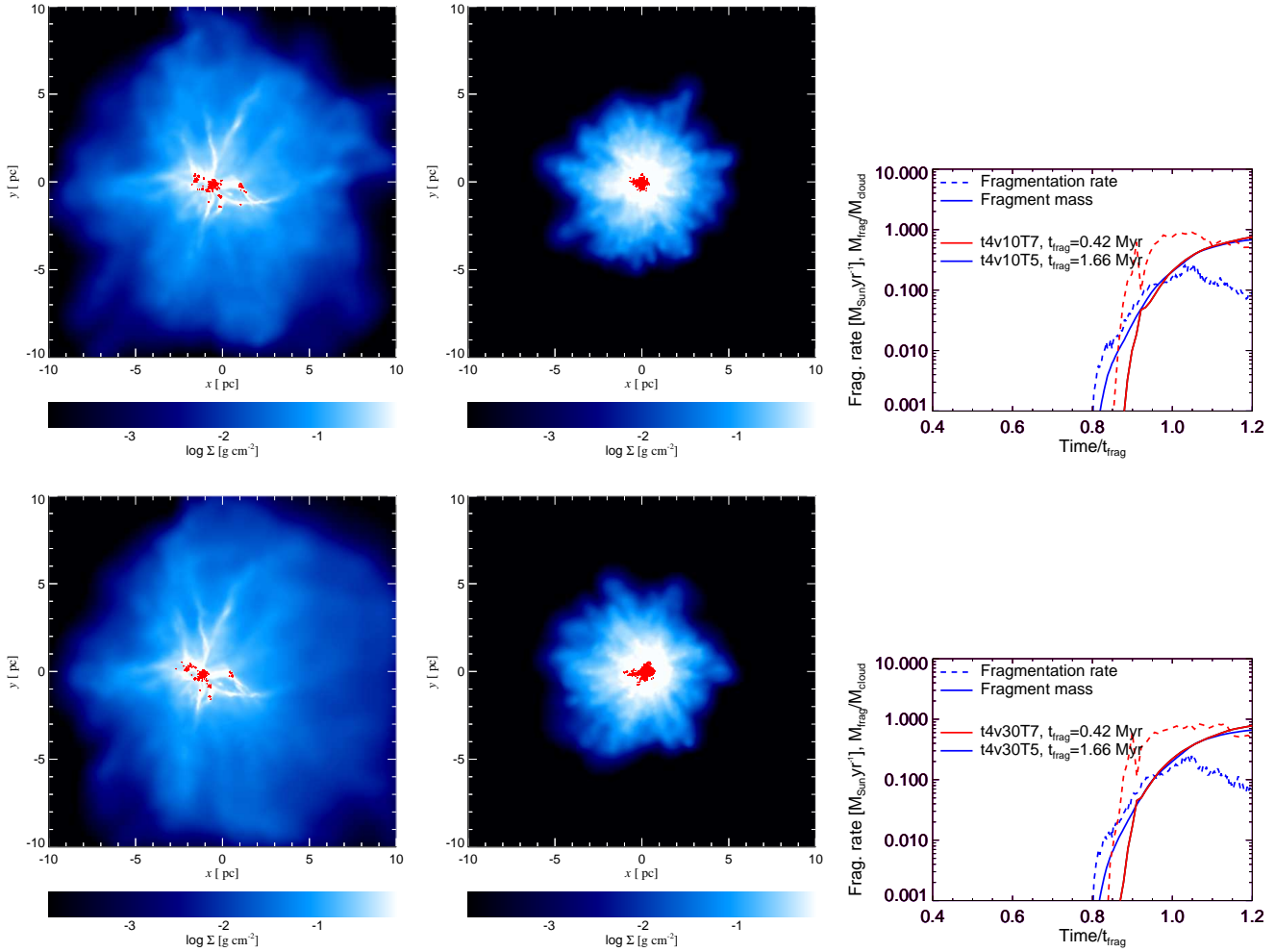


**Figure 7.** Morphology and time evolution of moving cloud models with lateral velocities of 10 km/s (top row) and 30 km/s (bottom row). Left column shows models with  $T_{\text{ISM}} = 10^5$  K, i.e. uncompressed clouds, middle column show clouds compressed with  $T_{\text{ISM}} = 10^7$  K (both at  $t = t_{\text{frag}}$ , right column shows the time evolution scaled to the fragmentation time. The ISM moves to the right in all left- and middle-column plots.

models in this group are essentially a form of the standard “blob test” for hydrodynamic codes (Nakamura et al. 2006; Agertz et al. 2007; Read & Hayfield 2012), except that the cloud is turbulent. The timescale of cloud destruction in such a system is (Agerz et al. 2007)

$$t_{\text{dest}} \sim 1.6 \times \frac{2R_{\text{cl}}}{v_{\text{lat}}} \left( \frac{\rho_{\text{cl}}}{\rho_{\text{ISM}}} \right)^{1/2} \sim 12.5 M_5^{1/2} R_{10}^{-1/2} v_{100}^{-1} \text{Myr}, \quad (18)$$

where  $v_{100} = v_{\text{lat}}/100$  km/s. We see that the clouds should not be destroyed by shear on the timescales relevant for our models, especially when the post-shock gas further compresses the cloud.

For numerical reasons, we set up the cloud as static, with the ISM moving past it at a uniform velocity  $v_{\text{lat}}$  in the positive X direction. We consider four ISM velocities:  $v_{\text{lat}} = 10, 30, 100$  and  $300$  km s $^{-1}$ . Direct acceleration of the cloud is important only in the fastest case, where the cloud is accelerated to a velocity of order  $\sigma_{\text{turb}}$  in  $\sim 0.8$  Myr (McKee et al. 1978); in the other cases,  $t_{\text{accel}} \gg t_{\text{dyn}}$ .

The results of these models are presented in Figures

7 (cases with  $v = 10$  and  $30$  km/s) and 8 ( $v = 100$  and  $300$  km/s). The first two columns in each figure show the morphology of these models at  $t = t_{\text{frag}}$ . In all the plots, the ISM is moving to the right. Each row represents a different lateral velocity, while the left and middle columns represent uncompressed and compressed models, respectively.

There is an immediately obvious qualitative difference between the T5 and T7 models, namely that T5 models fragment closer to the leading (left) edge of the cloud, while the T7 models fragment closer to the trailing (right) edge. This is easy to understand once we consider how shockwaves propagate through the clouds in various cases. In models t4v10T5 and t4v30T5, there is no discernible shockwave, since the lateral velocity is  $v_{\text{lat}} \ll \sigma_{\text{turb}} (\rho_{\text{cl}}/\rho_{\text{ISM}})^{1/2} \simeq 130$  km/s. The morphology of the fragmenting central regions is identical to those of the static cloud, and the parameters of fragmentation are almost identical as well (see Table 1): first sink particles appear at  $t = 1.33$  Myr in both models; the fragmentation timescale is also identical,  $t_{\text{frag}} = 1.66$  Myr, slightly smaller than in the static model (1.78 Myr). This discrepancy arises because some of the

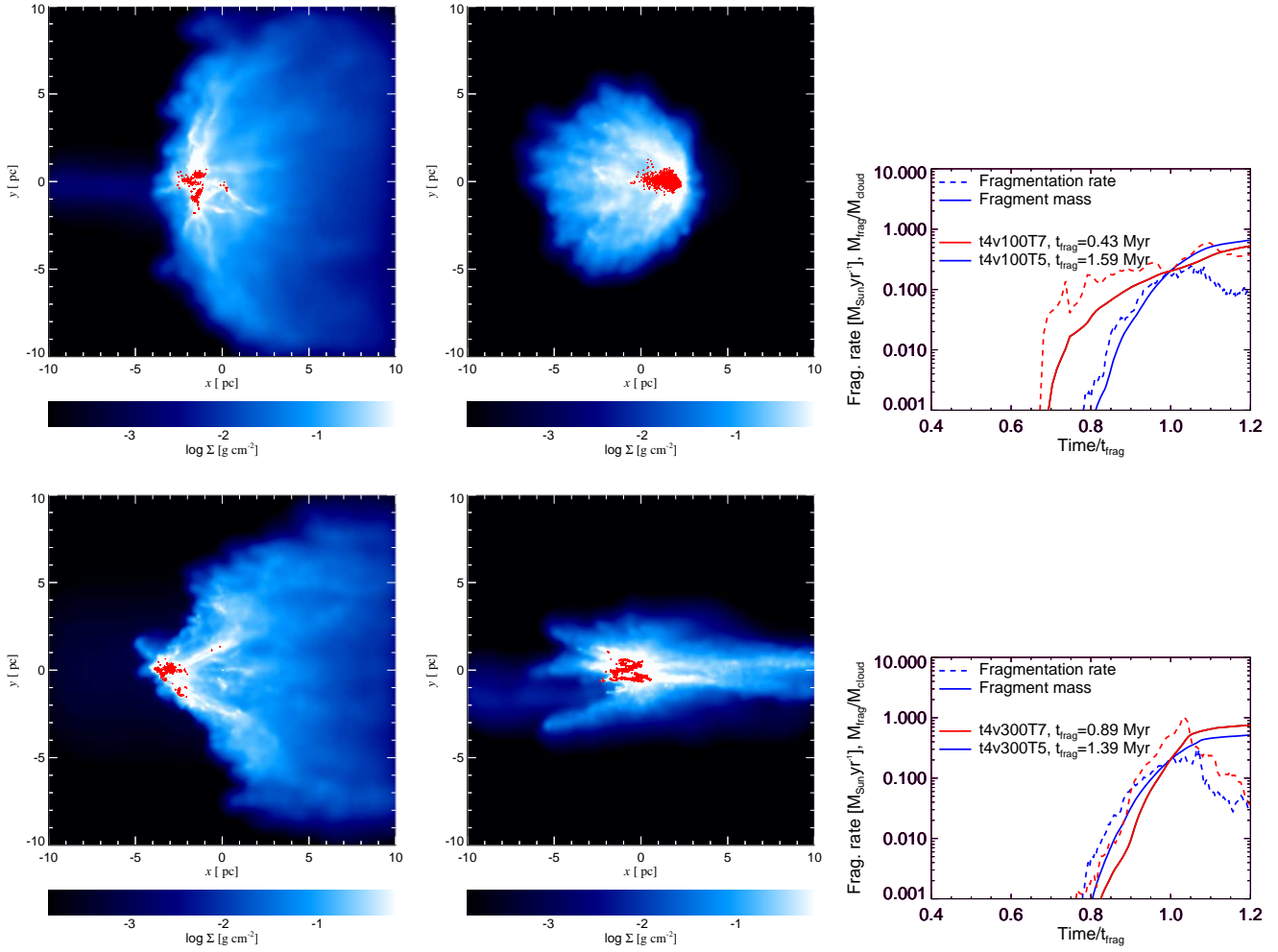


**Figure 8.** Same as Figure 7, but for models moving with 100 km/s (top row) and 300 km/s (bottom row).

cloud material is removed and joins the ISM, so the mass of the cloud drops and a lower total sink particle mass is required to bring the mass fraction up to 20%. Cloud ablation and slight compression along the leading edge also leads to the sink particle cluster appearing off-centre and to the half-mass radius of the cloud being much smaller (2.68 pc versus 4.26 pc in model t4T5).

In the higher velocity models, t4v100T5 and t4v300T5 (Figure 8, left column), the shockwave produced by the lateral motion of the ISM affects the cloud significantly. The shockwave moving through the cloud has a velocity comparable to or larger than the characteristic turbulent velocity, and so the cloud begins to break apart (as in the standard “blob test” Agertz et al. 2007). Fragmentation is accelerated by the shockwave, with first sink particles appearing at  $t = 1.23$  Myr and  $t = 1.08$  Myr in the v100 and v300 models, respectively, and occurs along the leading edge of the cloud. In particular, in the v300 model the shockwave enhances gas compression by  $\sim 20\%$ , so that the sink particles reach 20% by mass at only  $t_{\text{frag}} = 1.39$  Myr (in model v100,  $t_{\text{frag}} = 1.59$  Myr). The increasing importance of cloud ablation is also evident when considering the half-mass radii, which also increase with increasing lateral velocity. In both

models, the faint line of material visible on the left is the extended tail of the cloud arriving through the periodic boundary. The density of this tail is low enough to be insignificant for the evolution of the cloud.

The compressed models show different behaviour, because there is always a shockwave moving in through the cloud. Once again, the low velocity models evolve similarly to their static analogues, with both the time of appearance of the first sinks (0.36 Myr) and fragmentation time ( $t_{\text{frag}} = 0.42$  Myr) the same as in model t4T7. Faster motion (model t4v100T7) produces noticeable change in that the shockwave is anisotropic, moving in faster from the leading (left-hand) side, resulting in maximum compression in the trailing side of the cloud and more fragments forming there. The fragments also start forming earlier, at  $t = 0.29$  Myr, but  $t_{\text{frag}} = 0.43$  Myr is the same as in previous models. The fastest cloud, v300, is disrupted by the shockwave and so fragmentation is actually delayed, with first sink particles forming at  $t = 0.6$  Myr and  $t_{\text{frag}} = 0.89$ .

The right-hand columns of Figures 7 and 8 show the time evolution of fragmentation in the eight models. All four uncompressed models (blue lines) evolve similarly, with first sinks appearing at around  $0.8t_{\text{frag}}$ , the fragmentation rate

increasing up to  $\sim 0.2M_{\odot} \text{ yr}^{-1}$  and then dropping. Only in the fastest-moving model the fragmentation rate drops more significantly due to rapid removal of gas from the cloud. The two slow-moving compressed models evolve very similarly to the static compressed one (t4T7, compare the left panel in Figure 6), with a maximum fragmentation rate reaching  $\sim 1M_{\odot} \text{ yr}^{-1}$  at  $t \simeq t_{\text{frag}}$  before dropping slightly. In the v100 model (Figure 8, top right panel, red lines), fragmentation starts earlier, at  $t \simeq 0.65t_{\text{frag}}$  and proceeds more slowly, with fragmentation rate staying at  $\sim 0.3M_{\odot} \text{ yr}^{-1}$ . This happens because the anisotropic shockwave creates conditions for fragmentation as it moves through the cloud; this is evident from the elongated shape of the sink particle cluster (top middle panel). Finally, the compressed v300 model (Figure 8, bottom right panel, red lines) evolves superficially similarly to the uncompressed model, because the evolution is governed more by the shear than the isotropic compression.

## 6 DISCUSSION

Our simulations show that, under idealised conditions, high external pressure has a dominant effect on the collapse and fragmentation of a molecular cloud. Cloud fragmentation into pre-stellar cores is significantly accelerated in a compressed cloud, more than a simple pressure balance argument would suggest. Furthermore, even a highly turbulent cloud, which would be unbound without external confinement, is crushed and fragments in a very similar fashion to the low-turbulence analogue. In a similar fashion, cloud rotation is also unable to counteract external compression, although fragments form in qualitatively different locations in rotating clouds. Accelerated fragmentation leads to a larger fraction of the initial cloud mass converted into pre-stellar cores. Models of moving clouds show that the influence of low shear velocities ( $v_{\text{lat}} \ll 100 \text{ km/s}$ ) upon cloud evolution is minimal, but ram pressure caused by large velocity dominates over isotropic pressure and disrupts the cloud as it fragments.

We consider the general implications of these results below, in Section 6.1. We discuss the effect of external pressure upon cloud dispersal and formation of compact star clusters in Sections 6.2 and 6.3. On larger scales, our results support the possibility of positive AGN feedback (Section 6.4) and are consistent with other models of star formation enhancement or triggering by pressure (Section 6.5). Finally, we briefly review the validity of assumptions made in this work and discuss the possible improvements to the models in Section 6.6.

### 6.1 Cloud confinement

In all models of compressed clouds, the time evolution is almost identical. The integrated fragmentation parameters - the onset of fragmentation, the fragmentation rate and the timescale for a given fraction of the cloud to be transformed into sink particles - are hardly affected by differences in initial conditions, environment and cloud morphology. The only noticeable difference is that the rotating cloud models have lower mean sink particle mass, but the lack of detailed

star formation physics in our simulations prevents us from drawing significant conclusions regarding this property.

This similarity suggests that as long as external compression dominates over other sources of confinement, such as gravity or shock due to shearing motion, cloud fragmentation is governed almost exclusively by this compression. Furthermore, the acceleration of fragmentation is greater than the analytical estimate based on pressure balance predicts; this enhancement is due to instabilities enhancing the density contrast within the cloud.

Empirically, the increase of total (external + gravitational) pressure by a factor of  $11.4/1.4 \simeq 8$  leads to an increase in the fragmentation rate by a factor  $\sim 10$ , suggesting an almost linear relationship. However, we cannot constrain it further without a wider range of simulations, which are beyond the scope of this paper.

The results of even these idealised simulations reveal that external pressure can have an important, even dominating effect upon molecular cloud evolution. This effect should be accounted for in subgrid prescriptions of large-scale simulations. Typically, the timescale (and, equivalently, rate) of star formation in these prescriptions is governed by gas density only (Springel & Hernquist 2003; Fujita et al. 2003). Instead, they should take the surrounding hot gas pressure into account. In grid codes and some SPH codes (e.g., Springel & Hernquist 2003), cold and hot gas can be present in the same computational element, in which case the hot phase pressure change can be used when calculating the star formation rate in the cold component. In models where the cold phase is resolved with separate particles, the pressure of hot gas surrounding a particular cold gas clump should be used instead.

### 6.2 Formation of stars and parent cloud evolution

In most compressed cloud models, cloud fragmentation is enhanced by the shockwave moving in through the cloud together with the RM instabilities further increasing the density contrast. The shockwave only appears because we assume that the ISM pressure increases on a timescale shorter than the dynamical time of the cloud, so that the cloud does not have time to contract as a whole. Nevertheless, the confinement of cold gas would happen even in the case of gradual ISM density increase; Elmegreen & Efremov (1997) investigated such a situation, finding a higher star formation rate in clouds that virialize under high external pressure. Our simulation t10T7, with a highly turbulent cloud in approximate pressure equilibrium with its surroundings, where the shockwave would be weak, also shows significantly enhanced fragmentation. Therefore, the acceleration of star formation should be present independently of the existence of a shockwave. In the rotating compressed cloud model, sink particles appear in the shocked gas confined to the outskirts of the cloud. The similarity of this fragmentation rate to that of the static cloud depends on the initially uniform cloud density. In a more realistic cloud with a centrally-peaked density distribution, we would expect lower fragmentation rate. Since most molecular clouds should have nonzero angular momentum, the fragmentation rates we find should be taken as upper limits.

The overall sink particle formation rate in our compressed models is  $\sim 10$  times larger than in uncompressed

clouds. Since the fraction of pre-stellar core mass that ends up in a star is independent of core mass (Matzner & McKee 2000), the star formation rate should follow the same trend. This increase is larger than the scatter in the KS relation ( $\sigma_{\text{KS}} \simeq 0.2 - 0.3$  dex, Bigiel et al. 2008), so it should be detectable. There is some evidence that starburst galaxies have  $\sim 3 - 4$  times higher SFR surface densities at the same gas surface densities, and correspondingly shorter depletion timescales of the cold gas (García-Burillo et al. 2012). This finding is consistent with the suggestion that starbursts as a whole can be triggered by increased external pressure (Zubovas et al. 2013). A connection between higher star formation rate and external pressure was also found in resolved star-forming regions of M82 (Keto et al. 2005).

Stellar feedback, not included in our simulations, affects the properties of the forming stellar population. Young massive stars heat their surroundings, increasing the Jeans' mass and reducing the fragmentation rate (Bate 2009; Offner et al. 2009), leading to a top-heavy mass function (Krumholz et al. 2011; Bate 2012). Other forms of stellar feedback, such as prestellar outflows (Krumholz & Matzner 2009) and radiation pressure (Fall et al. 2010), also tend to increase the mean stellar mass. In our compressed cloud simulations, fragmentation happens much more rapidly, therefore more sink particles may form before radiative heating is able to shut off further fragmentation. On the other hand, external pressure confines the gas for longer, so the fragments can grow to much larger masses than in unconfined clouds. We cannot say which of the two processes is more important and how different the mass functions of compressed and uncompressed clouds would be without further simulations.

The global cloud dynamics is also affected by stellar feedback. Outflows driven by photoionization can potentially remove a significant fraction - more than 10% - of the cloud mass (Wang et al. 2010; Dale et al. 2012), leaving it and the nascent star cluster more prone to destruction (Dale et al. 2012; Pfalzner 2011). The effects of prestellar outflows (Krumholz et al. 2012), stellar winds (Dale et al. 2013) and radiation pressure (Krumholz & Matzner 2009) are also significant. In particular, radiation pressure is probably the primary mode of disruption of massive molecular clouds (Murray et al. 2010) and can drive significant turbulence (Krumholz et al. 2012). Supernova explosions begin  $\sim 3$  Myr after the formation of first stars and disperse most of the cloud gas within  $\sim 6$  Myr (Rogers & Pittard 2013). All of these effects can also trigger subsequent star formation by compressing the gas in other parts of the cloud (Dale et al. 2007; Koenig et al. 2012, also see Section 6.5.2 below). Ultimately, the star formation rate might be determined by self-regulation, whereby turbulent and stellar feedback pressure counteract gravity (Thompson et al. 2005). In our model, external pressure aids gravity and must be compensated as well (see also Section 6.4). We plan to investigate the effects of stellar feedback in a future publication.

In addition to internal stellar feedback, molecular clouds may be destroyed by external effects. Galactic-scale numerical simulations show cloud lifetimes of a few to  $\sim 20$  Myr (Dobbs & Pringle 2013). It is not clear how this dynamical evolution would be affected by external pressure, if at all. On timescales comparable to, or shorter than, the dynamical lifetime, the cloud can evaporate due to heating by the

ISM (Cowie & McKee 1977). Equation (22) of that paper, when rescaled to the parameters of our model clouds, reads

$$t_{\text{evap}} \sim 40 M_5 R_{10}^{-1} T_7^{-5/2} \text{Myr}. \quad (19)$$

So we may expect the compressed cloud to lose only a small fraction of its material to evaporation during the time relevant in our simulations. On the other hand, if the cloud was compressed by a much hotter ISM, evaporation might take over ( $t_{\text{evap}} \simeq 1.3 \times 10^5$  yr at  $T_{\text{ISM}} = 10^8$  K) and destroy the cloud before any significant star formation takes place. Shear also destroys the cloud on a timescale  $t_{\text{dest}} \sim 12.5 M_5^{1/2} R_{10}^{-1/2} v_{100}^{-1}$  Myr (eq. 18). This timescale is longer than the fragmentation timescales of all our models so long as  $v_{\text{lat}} < 600$  km/s. For less massive and/or more diffuse clouds, however, the destruction timescale is shorter and disruption due to shear might become the dominant mechanism, preventing rapid star formation. In addition, there are other processes that affect the cloud destruction timescale: a smoother density gradient increases this timescale (Nakamura et al. 2006), while turbulent motions in the post-shock ISM decrease it (Pittard et al. 2009).

Another result of cloud-shockwave interaction, as in blob tests, is that the cloud expands laterally behind the shockwave and thus becomes more susceptible to other forms of quasar feedback (Hopkins & Elvis 2010), enhancing the quenching effect that AGN activity can have upon star formation. We do not find this behaviour in our models for three reasons. First of all, we do not model the initial shockwave interaction with the cloud; however, the evolution of the fastest shearing cloud model, t4v300, is significantly affected by the shear-induced shockwave, so a similar effect might be expected. Secondly, the timescale of expansion is similar to the cloud crushing timescale, and our clouds evolve faster than this. Finally, the presence of isotropic pressure behind the shock helps confine the cloud, and further compresses it in the T7 model, preventing expansion and dispersal.

### 6.3 Evolution of star clusters

The sink particles tend to form in a single clump in all non-rotating models except v300. The clump rapidly relaxes and the sink particles appear to stay together in a cluster. In order to understand the subsequent evolution of this cluster, we plot, in Figure 9, the time evolution of the virial parameter  $\alpha_{\text{vir}} = E_{\text{kin}}/|E_{\text{g}}|$  of the sink particles for the non-shearing (top panel) and shearing models (bottom panel). In all pairs of models, the dashed line shows compressed clouds and solid line shows uncompressed ones. In all models, the sink particles are at first strongly unbound ( $\alpha_{\text{vir}} > 1$ ), but the virial parameter rapidly decreases, falling below 1 around  $t = t_{\text{frag}}$ . The only models which retain a formally unbound sink particle population throughout are t10T5, as one might naively expect, and t4v100T5, where the cloud disrupts as it is forming the clusters. After  $t_{\text{frag}}$ , the virial parameter increases in most models; this represents the fragmentation of a single sink particle cluster into subclusters, which disperse, since sink particles are not affected by surrounding gas pressure. Some models, such as t4 and t2.8r4.2 pairs, keep globally bound sink particle clusters throughout the simulation, but this is not a common occurrence, especially when shear is considered. Comparing



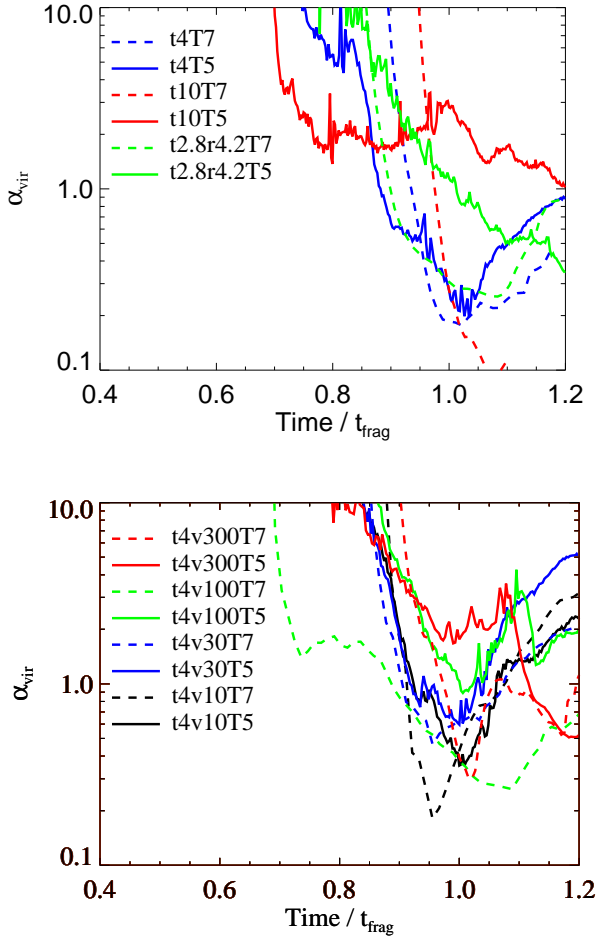


**Figure 9.** Virial parameter  $\alpha$  of the sink particles in the six models without shear (top) and eight models with shear (bottom). Solid lines correspond to uncompressed models, dashed lines represent compressed clouds. In the top panel, blue lines are low-turbulence models, red lines are high-turbulence while green lines are rotating models. In the bottom panel, the blue, red, green and black lines correspond to v10, v30, v100 and v300 models, respectively.

the compressed and uncompressed models in each pair, we see that in most cases, compressed clouds tend to have somewhat lower virial parameters. This suggests that compressed cloud are somewhat, but not significantly, more likely to form bound star clusters than uncompressed ones. Such clusters are then less likely to disperse due to internal motions soon after the parent cloud disperses (so-called “infant mortality”; Lada & Lada 2003, Section 5.2).

The sink particle clusters formed in the static cloud simulations have visually similar density profiles (Figure 3, right panel), but their half-mass radii differ, with model t4T5 having  $r_{h,sink} \simeq 0.79$  pc and model t4T7 having  $r_{h,sink} \simeq 0.26$  pc. This difference is caused by the high-density core present only in the compressed model and a low-density envelope present only in the uncompressed one. The difference is not large, so both clusters would appear very similar while young. However, their long-term evolution may be significantly different, especially because the

compressed cloud converts a larger fraction of its mass into sink particles (and, hence, stars). Both more massive (Kruijssen & Portegies Zwart 2009) and more compact (Spitzer 1987; Gieles & Baumgardt 2008) clusters can withstand the tidal field of the host galaxy more easily and lose a smaller fraction of their mass during evolution, so we may expect compressively-formed clusters to survive for longer. Since these clusters do not necessarily have very large masses, they may appear as compact star clusters (CSCs; Holtzman et al. 1992). These clusters are expected to form from molecular clouds that have been compacted by some process (Escala & Larson 2008; Larsen 2010), consistent with the picture presented in this paper. The higher star formation rate in the progenitor cloud coinciding with a more long-lived cluster is also consistent with observations that a larger fraction of stars stay in clusters in regions of galactic discs with higher star formation rate per unit area (Larsen & Richtler 2000). Similar arguments apply to our other models, both with and without shearing motion (see Table 1).

#### 6.4 Implications for positive AGN feedback

The main motivation of the simulations presented above is to validate the assumption that increased pressure leads to increased star formation rates, which is central to several models of positive AGN feedback (Zubovas et al. 2013; Silk 2005; Ciotti & Ostriker 2007). Such a connection requires, first of all, that external pressure should trigger and/or enhance molecular cloud fragmentation on timescales much shorter than the flow timescale of the AGN outflow. Otherwise, the decrease in outflow pressure as the outflow expands would preclude any significant enhancement of the galactic star formation rate. The flow timescale is of order several tens of Myr (King et al. 2011; Zubovas & King 2012); our results show that compressed molecular clouds evolve on much shorter timescales, so this requirement is satisfied.

In addition, the high fragmentation rate under compression must translate into a sustained high star formation rate. This requires that self-regulation of star formation produces a higher SFR at higher pressure. We may use the analytical model of Thompson et al. (2005) to show that this is expected. In that model, the star formation rate is set by the balance between pressure force from feedback processes (stellar radiation, winds and supernova explosions) and self-gravity of the gas. In our model, external pressure provides an extra force working in tandem with gravity:

$$F_{\text{grav}} + F_{\text{ISM}} = F_{\text{fb}}, \quad (20)$$

where the right-hand-side term is force from feedback. Assuming that all forces act isotropically, we can rewrite this equation in terms of pressures:

$$G\Sigma_{\text{tot}}^2 + P_{\text{ISM}} = \epsilon\dot{\Sigma}_*c, \quad (21)$$

where  $\Sigma_{\text{tot}} = \Sigma_g + \Sigma_*$  is the column density of cloud gas and stars. It follows from this relation that the star formation rate density increases when external confinement is present. Our results corroborate this finding, by showing that external pressure can easily confine clouds which have very high dynamical pressures (such as would be present in photoionized gas; see Section 6.1).

The shockwave of an AGN outflow can have a more

direct impact upon molecular clouds. Gray & Scannapieco (2011) found that AGN outflows can trigger vigorous star formation in primordial minihaloes, leading to formation of compact star clusters in systems that would otherwise not form stars at all. Although we do not model the passage of a shockwave around the cloud (see Section 6.5.2 for comments on other work addressing such issues), the increased fragmentation rate in our models is consistent with these results. On the other hand, star formation triggering by passage of supernova remnants requires a particular range of densities and SNR radii to work (Melioli et al. 2006); clouds that are too small are disrupted, while overly large clouds dissipate the shockwave too efficiently. A similar separation of various regimes may occur in the case of AGN feedback, but we cannot constrain these parameters without a larger study.

Therefore, our results support the models of positive AGN feedback due to outflows that can overpressurize the ambient gas and induce or increase star formation rates. In the future, we intend to run larger-scale simulations that will self-consistently treat the propagation of an AGN outflow and its effect on the dense clouds in a galaxy environment.

## 6.5 Other work

Several authors have considered the connection between star formation rates (both on GMC and on galactic scales) and the properties of the ambient medium, including pressure. We briefly summarize those results below and comment on their connection with our results.

### 6.5.1 External confinement of star forming regions

Recently, there has been mounting observational evidence that the immediate surroundings of the molecular clouds are an important element in their evolution. Observations of star-forming regions in M82 (Keto et al. 2005) show molecular clouds forming stars only when compressed by hot interstellar medium (ISM), but not on their own volition; this is the case even for parts of the same cloud which are otherwise indistinguishable observationally. At high redshift, many gas-rich galaxies show evidence of high ISM pressure (Swinbank et al. 2011), which correlates with the presence of starbursts. Observations of merger-triggered ULIRGs hint at star formation being triggered by molecular cloud infall into a high-pressure medium (Solomon et al. 1997). More recently, it was proposed that ISM pressure differences among M51, M33 and LMC are responsible for the properties of molecular clouds in those galaxies (Hughes et al. 2013).

From a theoretical standpoint, Jog & Solomon (1992) have investigated how GMCs react to an increase in HI cloud pressure due to galaxy collisions. Using analytical calculations, they predicted cloud crushing and enhanced star formation (see Section 3.1).

Elmegreen & Efremov (1997) proposed that all star clusters form by the same mechanism, with the primary difference in initial conditions being the external pressure affecting nascent molecular clouds. They suggest that globular clusters form in high-pressure environments, where the star formation efficiency is higher due to confinement. This result is similar to our findings, however we find that a sudden

increase in external pressure directly increases the fragmentation rate of the cloud, instead of simply preventing mass loss due to stellar feedback.

On galactic scales, Krumholz et al. (2009) suggested an explanation for the break in the star formation law (i.e. the proportionality between  $\Sigma_{\text{SFR}}$  and  $\Sigma_{\text{gas}}$ ) in galaxies based on external confinement of star-forming regions in dense environments. In this model, the high pressure of ambient galactic disc medium at large surface densities enhances star formation and leads to a steeper slope of the KS law than in lower-density systems. Although our simulations are not detailed enough to make predictions regarding the KS law, the results are consistent with this picture, except that we do not necessarily require high surface densities, merely the presence of an external pressure compressing the cloud.

### 6.5.2 Radiatively-driven implosion

Several aspects of our model are similar to radiation-driven implosion (RDI; Bertoldi 1989). This process has been investigated in great detail (Klein et al. 1980; Kessel-Deynet & Burkert 2003; Dale et al. 2007; Bisbas et al. 2011). Gas can be strongly compressed by either ionizing radiation from massive stars, passage of supernova shells, or both; molecular cloud fragmentation and star formation are enhanced as a result. Although we model a different kind of external pressure (almost isotropic and constant in time instead of directed and rapidly changing), the main result of increased pressure resulting in increased fragmentation rate is the same in both cases.

It is important to note that the observational evidence of RDI is inconclusive. Some molecular cloud surveys suggest that clouds with an increased star formation rate (compared with the background level) are affected by either passages of supernova shells (Preibisch & Zinnecker 1999) or ionizing radiation from nearby stellar clusters (Sugitani et al. 1989, 1991; Sugitani & Ogura 1994). The locations of intermediate- and low-mass stars in OB associations are consistent with their formation being triggered by the radiation of massive stars (Lee & Chen 2007). On the other hand, recent large surveys of young stellar objects located around infrared bubbles suggest that star formation on the edges of those bubbles is triggered by the collect-and-collapse model instead of RDI (Kendrew et al. 2012; Thompson et al. 2012). Despite these issues, it seems clear that RDI can enhance star formation in some environments and is a physically sound mechanism similar to our model.

## 6.6 Possible improvements to the model

In this paper, we are only interested in the basic dynamics, collapse and fragmentation of a turbulent cloud. Therefore, we purposefully neglected many physical processes that are relevant for the details of cloud evolution. We mentioned some of them, particularly stellar feedback, above; here we describe the other improvements we plan to make in the future.



### 6.6.1 Gas equation of state

The models presented in this paper use a heating-cooling function which includes most relevant processes. However, heating from protostars, both ionizing and non-ionizing, is not accounted for. Such heating can significantly change the mass function of stars (Bate 2009) and shut off further accretion and fragmentation after several Myr. We hope to expand our simulations with inclusion of these feedback mechanisms (radiative heating, photoionization, radiation pressure and stellar winds) in order to more properly simulate the properties of the star clusters forming in pressurized clouds.

### 6.6.2 Initial conditions and model scale

We make several simplifying assumptions both regarding the cloud and the ISM. First of all, we assume a uniform initial density of the cloud. Although turbulent velocities create an uneven density distribution very rapidly, more fundamental differences remain unexplored. In particular, a cloud with a  $\rho \propto R^{-2}$  density profile is more likely to form stars in the central regions. The confining effect of external pressure would remain, but triggering and acceleration of fragmentation would be mitigated. On the other hand, clouds with smoother boundaries are more stable against disruption due to shear (Nakamura et al. 2006) and would presumably be able to fragment for longer without dispersing.

Real molecular clouds have more complex density profiles. Ideally, the simulation should follow the molecular cloud assembly as well, because clouds exchange material with their surroundings throughout their  $\sim 5 - 20$  Myr lifetimes (e.g. Dobbs & Pringle 2013; Bournaud et al. 2013). In order to follow this process, the simulation volume should encompass a region of linear size  $l \sim 100$  pc, so that the assembly and evolution of a whole cloud complex can be followed (Wilson et al. 2003).

The hot ISM should also be implemented in a more realistic way, with turbulent motions and uneven evolving density structure. More importantly, the passage of the ISM shock around the cloud and its HI envelope can have different effects from those of the uniform ISM, even though the time for the ISM to envelope the cloud is much shorter than the cloud crushing timescale.

Eventually, we plan to run a simulation tracking a significant part of the whole galaxy. Such a simulation would allow for self-consistent formation of molecular clouds and driving of the AGN outflow (or any other process which generates increased external pressure). Unfortunately, at this scale, a feasible simulation would have a mass resolution of order  $10^3 M_\odot$  or worse, preventing one from investigating the details of cloud evolution. A balanced approach, combining insights from detailed small-scale simulations with the galactic context gleaned from large scale models, is needed.

### 6.6.3 Driving of turbulence

Currently, turbulent velocities are only implemented in the initial conditions of the models. This leads to a decay of turbulent power on the dynamical timescale of the cloud; this is a common feature of similar models (see, e.g., Bate et al. 2003). Therefore, our results become unrealistic after at

most one dynamical time independently of any other numerical inaccuracies. The decaying turbulence leads to an increase in fragmentation rate, especially in the uncompressed high-turbulence model (t10T5). Both star formation feedback (Krumholz et al. 2006) and accretion of external material (Klessen & Hennebelle 2010) maintain turbulent motions within the cloud, and both processes probably have similar relative importance (Goldbaum et al. 2011), so these processes should be included in more long-term simulations.

### 6.6.4 Numerical accuracy

We used sink particles in our simulations partly for convenience of analysis and partly in order to speed up the calculations. To test the importance of this approximation, we ran a simulation identical to t4T5, but without sink particles. We find that the global evolution of the cloud is identical between the two runs, but the model without sink particles retains more structure in the dense clumps than the sink particle cluster in t4T5. We conclude that the presence of sink particles does not affect our overall conclusions.

We also ran a simulation at higher resolution, using  $N = 4 \times 10^6$  particles instead of  $10^6$ . As expected, we find more small-scale clumps and filaments in the higher resolution model. The first sink particles appear slightly later, at  $t = 1.32$  Myr instead of 1.26 Myr. Overall, there is very little difference in the large-scale cloud evolution. Therefore, we conclude that our simulations are numerically converged.

The choice of hot-phase ISM density of  $1 \text{ cm}^{-3}$  is motivated by numerical considerations: higher density leads to more particles in the ISM and higher computational costs, while lower density reduces resolution and can lead to unwanted low-particle-number effects. Higher ISM temperature may lead to cloud evaporation on timescales comparable to fragmentation (see Section 6.3), but otherwise there should be no physical difference between pressure caused by a high-density ISM and a proportionately more diffuse, but hotter, ISM. Nevertheless, we intend to check for possible numerical differences in the future.

## 7 CONCLUSION

In this paper, we presented results of numerical simulations following the collapse and fragmentation of spherical turbulent molecular clouds under different external ISM pressures. Our idealized initial conditions contain spherical clouds with mass  $10^5 M_\odot$ , radius 10 pc and uniform density. Each cloud gas has an initial turbulent velocity spectrum with characteristic velocity of either 4 or 10 km/s to mimic self-gravitating and gravitationally unbound clouds, respectively. The ambient ISM pressure is either  $P_{\text{ISM}} = 10^5$  or  $10^7 \text{ K cm}^{-3}$ ; the lower value is similar to typical ISM pressures and does not affect cloud evolution, while the higher one significantly compresses the cloud. We consider the effects of pressure upon static and rotating clouds, as well as clouds moving with various lateral velocities w.r.t. the surrounding ISM.

The following are the main results:

- (i) The compressed clouds collapse and fragment much more rapidly and efficiently than the uncompressed ones.

The ratio between the times of comparable evolutionary state, i.e. the effective dynamical times of the uncompressed and compressed systems, is larger than the analytically predicted  $t'_{\text{dyn}}/t_{\text{dyn}} = (1 + P_{\text{ISM}}/P_{\text{cl}})^{-1/2}$ . The difference arises due to instabilities which follow behind the shockwave into the compressed clouds, enhance the density contrasts there and thus promote faster fragmentation. This result shows that external pressure can both accelerate star formation by compacting the cloud, and trigger star formation by promoting density contrasts.

(ii) The fragmentation rate in the cloud rapidly attains a constant value. This value, and presumably the corresponding star formation rate, is approximately linearly proportional to the total (virial plus external) pressure affecting the cloud. This proportionality can be used in subgrid models in larger simulations, thus accounting for the effects of increased ambient pressure around star forming regions.

(iii) Even high turbulence is unable to withstand the external pressure. The compressed clouds evolve in an almost identical fashion despite the difference in characteristic turbulent velocity. This confirms that external pressure can trigger star formation in regions that would otherwise have dispersed. Furthermore, it shows that external compression can confine clouds that would be destroyed by stellar feedback and allow for star formation to continue even after the first massive stars heat up the cloud.

(iv) Cloud rotation changes the morphology of the forming sink particle cluster, but not the time evolution of the fragmentation rate or fragment mass.

(v) The shearing motion of the cloud w.r.t. the surrounding ISM has a number of small effects. The cloud is ablated and progressively destroyed, reducing the final mass of the star cluster. Shear affects the shockwave driven into the cloud in compressed models, and can create a shockwave in uncompressed ones, provided that the shear velocity is large enough. The location of most vigorous fragmentation is affected by shear differently for different models: uncompressed clouds experience more fragmentation in the leading side, while compressed clouds fragment in the trailing part.

(vi) The sink particle clusters forming in compressed clouds are slightly more bound, more compact and more massive than those forming in the uncompressed clouds. This suggests that clusters formed in compressed clouds are more likely to survive as bound objects.

All together, these results indicate that external pressure has a strong effect on the evolution of cold-phase ISM and star formation. Not only passing shock fronts (such as supernova shells), but also large-scale isotropic pressure is important and should be included in models of galaxy evolution. More quantitative predictions require larger and more detailed simulations, which we plan to perform in the future.

## ACKNOWLEDGMENTS

We thank the anonymous referee for invaluable and extensive comments on the manuscript, which led to significant improvement of the paper. We thank Vidas Vansevicius, Sergei Nayakshin, Donatas Narbutis and Walter Dehnen for helpful discussions. KZ acknowledges the UK STFC for support in the form of a postdoctoral research position at the

University of Leicester. This work was funded by the Research Council of Lithuania grant no. PRO-15/2012.

Numerical simulations presented in this work were carried out on two computing clusters. Computations were performed on resources at the High Performance Computing Center HPC Sauletekis in Vilnius University Faculty of Physics. This research also used the ALICE High Performance Computing Facility at the University of Leicester. Some resources on ALICE form part of the DiRAC Facility jointly funded by STFC and the Large Facilities Capital Fund of BIS.

## REFERENCES

- Abramova O. V., Zasov A. V., 2008, *Astronomy Reports*, 52, 257
- Agertz O., Moore B., Stadel J., Potter D., Miniati F., Read J., Mayer L., Gawryszczak A., Kravtsov A., Nordlund Å., Pearce F., Quilis V., Rudd D., Springel V., Stone J., Tasker E., Teyssier R., Wadsley J., Walder R., 2007, *MNRAS*, 380, 963
- Allen L., Megeath S. T., Gutermuth R., Myers P. C., Wolk S., Adams F. C., Muzerolle J., Young E., Pipher J. L., 2007, *Protostars and Planets V*, pp 361–376
- Alves J., Lombardi M., Lada C. J., 2007, *A&A*, 462, L17
- Bastian N., Konstantopoulos I. S., Trancho G., Weisz D. R., Larsen S. S., Fouesneau M., Kaschinski C. B., Gieles M., 2012a, *A&A*, 541, A25
- Bastian N., Adamo A., Gieles M., Silva-Villa E., Lamers H. J. G. L. M., Larsen S. S., Smith L. J., Konstantopoulos I. S., Zackrisson E., 2012b, *MNRAS*, 419, 2606
- Bate M. R., 2009, *MNRAS*, 392, 1363
- Bate M. R., 2012, *MNRAS*, 419, 3115
- Bate M. R., Bonnell I. A., Bromm V., 2003, *MNRAS*, 339, 577
- Baumgardt H., Kroupa P., 2007, *MNRAS*, 380, 1589
- Begelman M. C., Cioffi D. F., 1989, *ApJL*, 345, L21
- Bekki K., Couch W. J., 2003, *ApJL*, 596, L13
- Bekki K., Forbes D. A., Beasley M. A., Couch W. J., 2002, *MNRAS*, 335, 1176
- Bertoldi F., 1989, *ApJ*, 346, 735
- Bigiel F., Leroy A., Walter F., Brinks E., de Blok W. J. G., Madore B., Thornley M. D., 2008, *AJ*, 136, 2846
- Bisbas T. G., Wünsch R., Whitworth A. P., Hubber D. A., Walch S., 2011, *ApJ*, 736, 142
- Bournaud F., Perret V., Renaud F., Dekel A., Elmegreen B. G., Elmegreen D. M., Teyssier R., Amram P., Daddi E., Duc P.-A., Elbaz D., Epinat B., Gabor J. M., Juneau S., Kraljic K., Le Floch' E., 2013, *ArXiv e-prints*
- Bressert E., Ginsburg A., Bally J., Battersby C., Longmore S., Testi L., 2012, *ApJL*, 758, L28
- Bryant P. M., Scoville N. Z., 1999, *AJ*, 117, 2632
- Ciotti L., Ostriker J. P., 2007, *ApJ*, 665, 1038
- Clark P. C., Bonnell I. A., Zinnecker H., Bate M. R., 2005, *MNRAS*, 359, 809
- Cowie L. L., McKee C. F., 1977, *ApJ*, 211, 135
- Dale J. E., Bonnell I., 2011, *MNRAS*, 414, 321
- Dale J. E., Bonnell I. A., Whitworth A. P., 2007, *MNRAS*, 375, 1291
- Dale J. E., Clark P. C., Bonnell I. A., 2007, *MNRAS*, 377, 535

- Dale J. E., Ercolano B., Bonnell I. A., 2012, *MNRAS*, 424, 377
- Dale J. E., Ngoumou J., Ercolano B., Bonnell I. A., 2013, *MNRAS*, 436, 3430
- Davies R. I., Sternberg A., Lehnert M. D., Tacconi-Garman L. E., 2005, *ApJ*, 633, 105
- Dobbs C. L., Pringle J. E., 2013, *MNRAS*, 432, 653
- Drouart G., De Breuck C., Vernet J., Seymour N., Lehnert M., Barthel P., Bauer F. E., Ibar E., Galametz A., Haas M., Hatch N., Mullaney J. R., Nesvadba N., Rocca-Volmerange B., Rottgering H. J. A., Stern D., Wylezalek D., 2014, *ArXiv e-prints*
- Dubinski J., Narayan R., Phillips T. G., 1995, *ApJ*, 448, 226
- Elmegreen B. G., Efremov Y. N., 1997, *ApJ*, 480, 235
- Escala A., Larson R. B., 2008, *ApJL*, 685, L31
- Fabian A. C., 2012, *ARA&A*, 50, 455
- Fall S. M., Chandar R., 2012, *ApJ*, 752, 96
- Fall S. M., Krumholz M. R., Matzner C. D., 2010, *ApJL*, 710, L142
- Federrath C., Duval J., Klessen R. S., Schmidt W., Low M.-M. M., 2010, *Highlights of Astronomy*, 15, 404
- Feruglio C., Maiolino R., Piconcelli E., Menci N., Aussel H., Lamastra A., Fiore F., 2010, *A&A*, 518, L155+
- Fujita A., Martin C. L., Mac Low M.-M., Abel T., 2003, *ApJ*, 599, 50
- Gaibler V., Khochfar S., Krause M., Silk J., 2012, *MNRAS*, 425, 438
- García-Burillo S., Usero A., Alonso-Herrero A., Graciá-Carpio J., Pereira-Santaella M., Colina L., Planesas P., Arribas S., 2012, *A&A*, 539, A8
- Geyer M. P., Burkert A., 2001, *MNRAS*, 323, 988
- Gieles M., Baumgardt H., 2008, *MNRAS*, 389, L28
- Goldbaum N. J., Krumholz M. R., Matzner C. D., McKee C. F., 2011, *ApJ*, 738, 101
- Gray W. J., Scannapieco E., 2011, *ApJ*, 742, 100
- Hartmann L., Ballesteros-Paredes J., Bergin E. A., 2001, *ApJ*, 562, 852
- Hennebelle P., Falgarone E., 2012, *Astron.Astrophys.Rev.*, 20, 55
- Hobbs A., Nayakshin S., Power C., King A., 2011, *MNRAS*, 413, 2633
- Hobbs A., Read J., Power C., Cole D., 2013, *MNRAS*, 434, 1849
- Holtzman J. A., Faber S. M., Shaya E. J., Lauer T. R., Groth J., Hunter D. A., Baum W. A., Ewald S. P., Hester J. J., Light R. M., Lynds C. R., O'Neil Jr. E. J., Westphal J. A., 1992, *AJ*, 103, 691
- Hopkins P. F., Elvis M., 2010, *MNRAS*, 401, 7
- Hughes A., Meidt S. E., Colombo D., Schinnerer E., Pety J., Leroy A. K., Dobbs C. L., García-Burillo S., Thompson T. A., Dumas G., Schuster K. F., Kramer C., 2013, *ApJ*, 779, 46
- Inoue T., Inutsuka S.-i., 2008, *ApJ*, 687, 303
- Ishibashi W., Fabian A. C., 2012, *MNRAS*, 427, 2998
- Jog C. J., Solomon P. M., 1992, *ApJ*, 387, 152
- Kawamura A., Mizuno Y., Minamidani T., Filipović M. D., Staveley-Smith L., Kim S., Mizuno N., Onishi T., Mizuno A., Fukui Y., 2009, *ApJS*, 184, 1
- Kendrew S., Simpson R., Bressert E., Povich M. S., Sherman R., Lintott C. J., Robitaille T. P., Schawinski K., Wolf-Chase G., 2012, *ApJ*, 755, 71
- Kessel-Deynet O., Burkert A., 2003, *MNRAS*, 338, 545
- Keto E., Ho L. C., Lo K.-Y., 2005, *ApJ*, 635, 1062
- King A. R., Zubovas K., Power C., 2011, *MNRAS*, pp L263+
- Klein R. I., McKee C. F., Colella P., 1994, *ApJ*, 420, 213
- Klein R. I., Sandford II M. T., Whitaker R. W., 1980, *Sp.Sci.Rev.*, 27, 275
- Klessen R. S., Hennebelle P., 2010, *A&A*, 520, A17
- Koenig X. P., Leisawitz D. T., Benford D. J., Rebull L. M., Padgett D. L., Assef R. J., 2012, *ApJ*, 744, 130
- Kroupa P., Boily C. M., 2002, *MNRAS*, 336, 1188
- Kruijssen J. M. D., 2012, *MNRAS*, 426, 3008
- Kruijssen J. M. D., 2013, *ArXiv e-prints*
- Kruijssen J. M. D., Portegies Zwart S. F., 2009, *ApJL*, 698, L158
- Krumholz M. R., Dekel A., McKee C. F., 2012, *ApJ*, 745, 69
- Krumholz M. R., Klein R. I., McKee C. F., 2011, *ApJ*, 740, 74
- Krumholz M. R., Klein R. I., McKee C. F., 2012, *ApJ*, 754, 71
- Krumholz M. R., Matzner C. D., 2009, *ApJ*, 703, 1352
- Krumholz M. R., Matzner C. D., McKee C. F., 2006, *ApJ*, 653, 361
- Krumholz M. R., McKee C. F., Tumlinson J., 2009, *ApJ*, 699, 850
- Krumholz M. R., Tan J. C., 2007, *ApJ*, 654, 304
- Krumholz M. R., Thompson T. A., 2012, *ApJ*, 760, 155
- Krumholz M. R., Thompson T. A., 2013, *MNRAS*, 434, 2329
- Lada C. J., Lada E. A., 2003, *ARA&A*, 41, 57
- Larsen S. S., 2010, *Royal Society of London Philosophical Transactions Series A*, 368, 867
- Larsen S. S., Richtler T., 2000, *A&A*, 354, 836
- Larson R. B., 1981, *MNRAS*, 194, 809
- Lee H.-T., Chen W. P., 2007, *ApJ*, 657, 884
- Matzner C. D., McKee C. F., 2000, *ApJ*, 545, 364
- McKee C. F., Cowie L. L., 1977, *ApJ*, 215, 213
- McKee C. F., Cowie L. L., Ostriker J. P., 1978, *ApJL*, 219, L23
- McKee C. F., Ostriker E. C., 2007, *ARA&A*, 45, 565
- McNamara B. R., Nulsen P. E. J., 2007, *ARA&A*, 45, 117
- Melioli C., de Gouveia Dal Pino E. M., de La Reza R., Raga A., 2006, *MNRAS*, 373, 811
- Murray N., Quataert E., Thompson T. A., 2010, *ApJ*, 709, 191
- Nakamura F., McKee C. F., Klein R. I., Fisher R. T., 2006, *ApJS*, 164, 477
- Nayakshin S., Zubovas K., 2012, *MNRAS*, 427, 372
- Offner S. S. R., Klein R. I., McKee C. F., Krumholz M. R., 2009, *ApJ*, 703, 131
- Pfalzner S., 2011, *A&A*, 536, A90
- Pittard J. M., Falle S. A. E. G., Hartquist T. W., Dyson J. E., 2009, *MNRAS*, 394, 1351
- Preibisch T., Zinnecker H., 1999, *AJ*, 117, 2381
- Quinn P. J., Hernquist L., Fullagar D. P., 1993, *ApJ*, 403, 74
- Read J. I., Hayfield T., 2012, *MNRAS*, 422, 3037
- Read J. I., Hayfield T., Agertz O., 2010, *MNRAS*, 405, 1513
- Ricker P. M., 1998, *ApJ*, 496, 670
- Rogers H., Pittard J. M., 2013, *MNRAS*, 431, 1337

- Roman-Duval J., Jackson J. M., Heyer M., Rathborne J., Simon R., 2010, *ApJ*, 723, 492
- Sazonov S. Y., Ostriker J. P., Sunyaev R. A., 2004, *MNRAS*, 347, 144
- Scoville N. Z., Yun M. S., Bryant P. M., 1997, *ApJ*, 484, 702
- Silk J., 2005, *MNRAS*, 364, 1337
- Solomon P. M., Downes D., Radford S. J. E., Barrett J. W., 1997, *ApJ*, 478, 144
- Solomon P. M., Rivolo A. R., Barrett J., Yahil A., 1987, *ApJ*, 319, 730
- Spitzer L., 1978, Physical processes in the interstellar medium
- Spitzer L., 1987, Dynamical evolution of globular clusters
- Springel V., 2005, *MNRAS*, 364, 1105
- Springel V., Hernquist L., 2003, *MNRAS*, 339, 289
- Sugitani K., Fukui Y., Mizuni A., Ohashi N., 1989, *ApJL*, 342, L87
- Sugitani K., Fukui Y., Ogura K., 1991, *ApJS*, 77, 59
- Sugitani K., Ogura K., 1994, *ApJS*, 92, 163
- Swinbank A. M., Papadopoulos P. P., Cox P., Krips M., Ivison R. J., Smail I., Thomson A. P., Neri R., Richard J., Ebeling H., 2011, *ApJ*, 742, 11
- Thompson M. A., Urquhart J. S., Moore T. J. T., Morgan L. K., 2012, *MNRAS*, 421, 408
- Thompson T. A., Quataert E., Murray N., 2005, *ApJ*, 630, 167
- Wang P., Li Z.-Y., Abel T., Nakamura F., 2010, *ApJ*, 709, 27
- Williams J. P., McKee C. F., 1997, *ApJ*, 476, 166
- Wilson C. D., Scoville N., Madden S. C., Charmandaris V., 2003, *ApJ*, 599, 1049
- Wolfire M. G., McKee C. F., Hollenbach D., Tielens A. G. G. M., 2003, *ApJ*, 587, 278
- Zubovas K., King A., 2012, *ApJL*, 745, L34
- Zubovas K., King A. R., 2014, *MNRAS*, 439, 400
- Zubovas K., Nayakshin S., King A., Wilkinson M., 2013, *MNRAS*, 433, 3079